Physics – Uspekhi **51** (6) 551 – 576 (2008)

REVIEWS OF TOPICAL PROBLEMS PACS numbers: **47.87. – i**, 97.10.Gz, **97.80. – d**

The nature of accretion disks of close binary stars: overreflection instability and developed turbulence

A M Fridman, D V Bisikalo

DOI: 10.1070/PU2008v051n06ABEH006583

Contents

Abstract. The current status of the physics of accretion disks in close binary stars is reviewed, with an emphasis on the hydrodynamic overreflection instability, which is a factor leading to the accretion disk turbulence. The estimated turbulent viscosity coefficients are in good agreement with observations and explain the high angular momentum transfer rate and the measured accretion rate. Based on the observations, a power-law spectrum for the developed turbulence is obtained.

1. Introduction

Accretion disks are known to be objects with the maximum efficiency coefficient among all other objects in the Universe: their radiation energy varies from 6 to 30% of Mc^2, where M is the mass of an accretion disk and c is the speed of light (cf. 0.3% Mc^2 for nuclear reactions in the interior of a star). Until recently, the cause of such a high efficiency had been unknown.

A M Fridman Institute of Astronomy, Russian Academy of Sciences, ul. Pyatnitskaya 48, 119017 Moscow, Russian Federation
Tel. (7-495) 951 79 93
Fax (7-495) 230 20 81
E-mail: afridman@inasan.rssi.ru
Russian Research Center Kurchatov Institute, Institute of Physics of Stochastic Structures, pl. Kurchatova 1, 123182 Moscow, Russian Federation
D V Bisikalo Institute of Astronomy, Russian Academy of Sciences, ul. Pyatnitskaya 48, 119017 Moscow, Russian Federation
E-mail: bisikalo@inasan.ru

Received 28 February 2008
Uspekhi Fizicheskikh Nauk **178** (6) 577 – 604 (2008)
DOI: 10.3367/UFNr.0178.200806b.0577
Translated by Yu V Morozov and S D Danilov; edited by A M Semikhatov

Meanwhile, the results of observations suggest that accretion disks have abnormally high turbulent viscosity coefficients (9 – 11 orders of magnitude higher than molecular viscosity coefficients). This strong turbulence facilitates conversion of the kinetic energy of plasma incident on the accretion disk into the energy of radiation. What is then the cause of such well-developed turbulence in accretion disks?

This review was undertaken to find answers to this and related questions.

Accretion disks of close binary systems (CBSs) are not rare in the Universe. On the contrary, they rather frequently occur in our Galaxy because almost 80% of the stars arise in pairs (see, e.g., [1]). A star having a large mass completes its 'life journey' and turns into a compact object sooner than a lighter star. The end product of evolution may be either a white dwarf, a neutron star, or a black hole, depending on the mass. Its companion, the second star, grows in size during the same period. When its radius reaches the libration point, at which all forces except the pressure gradient are in equilibrium, the process of spillover and incidence of matter on the compact object (accretion) begins. For this reason, such an object is termed an accretor (also referred to as star 2 below), while the star losing mass is called a donor or star 1 (Fig. 1). The Roche approximation usually used in binary star studies is based on the following assumptions:

(1) the gravitational field of either star is strictly spherically symmetric;

(2) the orbits of both stars around their centers of mass are circular;

(3) self-rotations of the stars are synchronized with their orbiting by tidal forces, just as rotations in the Earth – Moon system are, the result being that we see only one side of the Moon.

We consider a binary star system with the distance A between their centers, the orbital angular velocity $\mathbf{\Omega}_{\rm orb}$, and

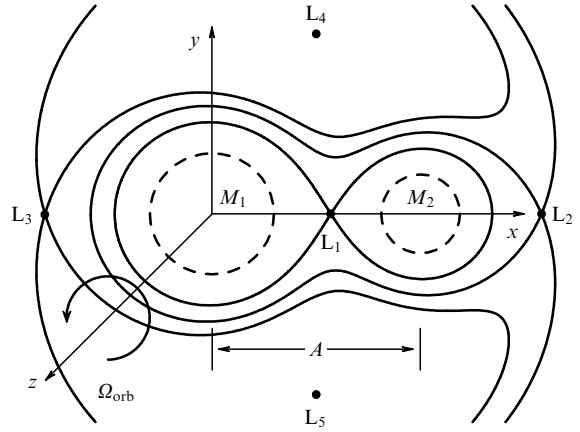

Figure 1. Equipotential Roche surfaces in the equatorial plane of a binary system with the mass ratio $q = M_2/M_1 = 0.5$. Libration points are marked as $L_1 - L_5$.

the orbital period $P_{\rm orb} = 2\pi/\Omega_{\rm orb}$. The components of the system, stars 1 and 2, have masses M_1 and M_2. We use a right-handed coordinate system rotating synchronously with the binary system. The origin of the coordinate system is at the center of star 1, the x axis is parallel to the line connecting the centers of the stars, and the z axis is parallel to the rotation axis (see Fig. 1).

The effect of rotation can be described in terms of classical mechanics [2] by introducing an additional term in the expression for the energy of a rotating body with mass M. This term depends only on the coordinates of the body and is proportional to the squared angular velocity: $-(1/2)M[\mathbf{\Omega}_{\rm orb} \times (\mathbf{r} - \mathbf{r}_{\rm c})]^2$, where $\mathbf{r}_{\rm c}$ is the radius vector of the centers of mass of the binary system. Such an additional term is called the centrifugal energy [2]. The gravity potential Φ of the field of forces in this coordinate system has the form

$$\Phi = -\frac{GM_1}{\sqrt{x^2+y^2+z^2}} - \frac{GM_2}{\sqrt{(x-A)^2+y^2+z^2}} - \frac{1}{2}\,\Omega_{\rm orb}^2\left[\left(x - A\,\frac{M_2}{M_1+M_2}\right)^2 + y^2\right], \qquad (1)$$

where G is the gravitational constant.

Examples of equipotential surfaces described by Eqn (1) are presented in Fig. 1. For large $-\Phi$, these surfaces are two spheroidal cavities that enclose the respective gravitating masses M_1 and M_2 (dashed circles in Fig. 1). As $-\Phi$ decreases, the surfaces broaden and come into contact at a point known as the first libration point. We note that the first libration point is usually referred to in the astrophysical literature as the inner Lagrange point L_1, even though this trend is in conflict with historic evidence, the first three libration points (L_1, L_2, L_3) having been discovered by Euler in 1767. Five years later (1772), Lagrange discovered the last two libration points (L_4, L_5) that are termed triangular libration points or Lagrange points in celestial mechanics.

Libration points are remarkable in that the sum of all three forces (two gravity forces of attraction to masses M_1 and M_2 and the centrifugal force) is equal to zero, $\nabla\Phi = 0$. The first three libration points are unstable: a probe particle placed at these points leaves them upon an infinitely small perturbation. At the same time, the Lagrange points L_4 and L_5 remain stable for the mass ratio of CBS components $q < 0.04$ [3], which enables particles to accumulate in them. This phenomenon has been observed in the solar system since 1906 when the family of Trojan asteroids was discovered in the vicinity of the triangular libration points in the Sun–Jupiter system. We note, however, that the condition $q < 0.04$ in the restricted three-body problem related to the solar system dynamics is invariably satisfied and the respective points L_4 and L_5 are stable. For close binary stars, the inverse inequality, $q > 0.04$, typically holds. This means that all five libration points in a CBS are unstable.

The region bounded by an equipotential surface containing the libration point L_1 is called the Roche lobe. This region plays an important role in the physics of binary stars because the size of a star cannot be substantially larger than the Roche lobe radius. When one of the stars fills up the entire Roche lobe, stellar matter begins to overflow into the Roche lobe of the accretor star through the vicinity of the point L_1 under the action of an unbalanced pressure force. If the accretor's radius is small, a large fraction of the inflowing material having an excessive angular momentum gives rise to the so-called accretion disk around the accretor star.

Observations of close binary stars (especially in the shortwave spectral region) give evidence of an intense flow of matter streaming to the accretor. Such a flow occurs solely under the condition that a large fraction of the angular momentum of the accretion plasma is transferred onto the outer parts of the disk. This requires an enormously high viscosity (9–11 orders of magnitude higher than the molecular viscosity), possible only in the case of well-developed turbulence in the accretion disk. The developed turbulence resulting from strong instability is not the sole mechanism by which the angular momentum is redistributed; other physical processes are supposed to operate to the same effect. The principal ones are the tidal interaction [4–6], spiral shock waves [7–10], convection [11–14], wind from an accretion disk, jets [15–18], the angular momentum transfer by propagating waves [19–21], and various instabilities of the accretion disk, such as magnetohydrodynamic [22–25], parametric [26, 27], and baroclinic [28–30]. Analysis of different modes of angular momentum transfer (see, e.g., Refs [31, 32]) indicates that all the above mechanisms encounter difficulties in explaining the accretion disk properties.

The best known and popular mechanism is the magnetorotational instability (MRI) [22]. However, it needs a magnetic field to be operative. Results of observations suggest the existence of many systems in which the field is so weak that it fails to manifest itself. For an MRI to develop, the field must be readily appreciable not only at the surface of the accretor star but also much farther from it (e.g., at a distance as large as the accretion disk radius). There are practically no such systems among CBSs. Consequently, the MRI mechanism is inapplicable.

Another crucial point is that the mechanism of angular momentum transfer must be operative in high-temperature disks. The fact is that the matter density in a disk being formed is low, which makes the process of radiative cooling inefficient. At the same time, the accretor star typically has a high temperature. For this reason, the equilibrium temperature of disk matter at the moment of its formation is also high.

The present review describes an efficacious mechanism of angular momentum transfer that we proposed in [33]; this mechanism operates in hot disks of close binary systems in the absence of a magnetic field.

2. Accretion disks in close binary stars

2.1 Background information

In a classical consideration, a CBS is assumed to have a critical surface whose occupation by one of the stars triggers mass exchange within the system. This surface is identified with the inner critical surface (Roche surface) in the restricted three-body problem. The exchange of matter occurs via the neighborhood of the libration point L_1 where the pressure gradient is not counterbalanced by the gravity force. The gasdynamics of matter efflux from the neighborhood of L_1 has been investigated by many authors. In a semianalytic approximation, the problem was first analyzed in [34] and [35]; its current interpretation and a review of topical issues can be found in reviews [36–38].

We follow up the fate of a gas after it passes the libration point L_1. As the gas moves away from L_1, its velocity increases under the action of an attractive force of the accretor star (star 2). Soon, the motion becomes essentially supersonic (see, e.g., Refs [35, 39]). Moreover, the Coriolis force diverts the stream of matter from the line connecting star centers. According to [35], the stream deflection angle ϑ_s is given by

$$\cos(2\vartheta_s) = -\frac{4}{3}\, g_\vartheta^{-1} + \sqrt{1 - \frac{8}{9}\, g_\vartheta^{-1}}\,,$$

where

$$g_\vartheta(q) = \left[\frac{q}{(x_{L_1}/A)^3} + \frac{1}{(1 - x_{L_1}/A)^3}\right](q+1)^{-1}\,.$$

The stream deflection angle ϑ_s depends on the component mass ratio alone. It can be seen from Fig. 2a that in the simplest case under consideration (disregarding stream interaction with the unaccreted gas), the rotation stream angle varies only insignificantly (in the range from $-28.4°$ to $-19.5°$).

The trajectory of the stream in a binary system is frequently considered in the ballistic approximation on the formal grounds that this approximation is permitted by the supersonic nature of the stream, which allows neglecting pressure effects. The equation of motion describing the trajectory of such a particle in the absence of a magnetic field and pressure effects can be written as

$$\frac{\mathrm{d}^2\mathbf{r}}{\mathrm{d}t^2} = -\nabla\Phi - 2\boldsymbol{\Omega} \times \frac{\mathrm{d}\mathbf{r}}{\mathrm{d}t}\,.$$

The results of the computation of trajectories in the orbital plane of a system with equal component masses ($q = 1$) are presented in Fig. 2b. Evidently, at low initial velocities,[1] all trajectories of particles are approximately identical and independent of the angle at which they enter the system.

It can be concluded from the analysis of trajectories that the stream passes close enough to the point mass, i.e., star 2 in the Roche approximation. The minimally attainable distance R_{min} between the trajectory of an individual particle and the center of the star for systems with different component mass ratios is shown in Fig. 2c [35]. In the range $0.05 < q < 1$, the value of R_{min} can be approximated with an accuracy of 1% by

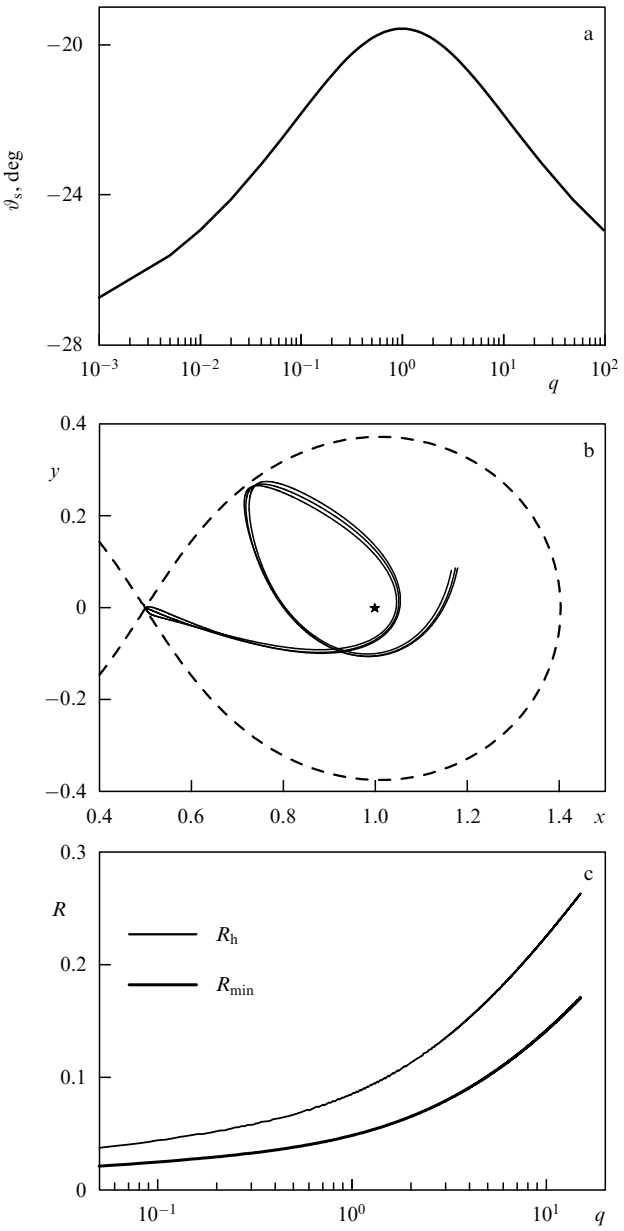

Figure 2. (a) The function $\vartheta_s(q)$ giving the stream deflection angle [35]. (b) Trajectories of particles in the orbital plane of a binary system with the component mass ratio $q = 1$; it was assumed for the purpose of computation that the particles escape from L_1 at a low speed $u = 0.03\sqrt{G(M_1 + M_2)/A}$ in the directions 0° and ±45° relative to the line connecting the centers of the components. (c) The minimal distance R_{min} between star 2 and a particle from L_1 during the first passage and the initial ring radius R_h as functions of the component mass ratio q.

the expression [38]

$$\frac{R_{min}}{A} = 0.0488 q^{-0.464}\,.$$

In binary systems with the second component radius $R_2 > R_{min}$, the stream of matter reaches the surface of the star. But when $R_2 < R_{min}$, the stream flow rounds the star and eventually intersects itself at a certain point (see trajectories in Fig. 2b). It is worth noting that the presence of intersecting trajectories in the system suggests strong interactions between gas streams, considering which in the ballistic approximation is incorrect. The complicated character of the interaction between the stream and the material of the circumbinary

[1] Here, the particle velocity is compared with the characteristic orbital velocity of the binary system, $\sqrt{G(M_1 + M_2)/A}$.

envelope requires solving the complete set of gasdynamic equations for the description of mass transfer in semidetached binary stars. Examples of such a description are given in Section 3. Here, following [35, 40], we qualitatively consider the flow pattern based on the analysis of probe particle trajectories.

We consider the angular momentum of a particle after it passes the point at which the trajectory intersects itself. Because the intersection point of the trajectories of probe particles is rather close to star 2, the effect of star 1 on the flow near the collision point can be disregarded. Hence, it may be assumed that the angular momentum of the gas element about star 2 is conserved. The minimal energy for a particle with a fixed angular momentum revolving around a point mass is reached at a circular orbit. Therefore, it can be expected that after collision, the gas forms a ring with a radius R_h around star 2. The gas in the ring rotates about star 2 with the azimuthal velocity v_ϕ estimated, under the assumption of the absence of pressure forces, from the balance between the centrifugal force v_ϕ^2/r and the gravitational attraction of the star GM_2/r^2. Equating them yields a gas ring obeying the Kepler rotation law $v_K = (GM_2/r)^{1/2}$. The angular momentum in such a ring increases in the centrifugal direction as $\sqrt{r}$.

The radius R_h of the initial ring can be found by the method in [35] as the distance to the accretor over which the stream of matter has the same tangential velocity as a particle in a closed periodic orbit passing through a given point. But this approach is too complicated for algorithmization. R_h can be determined with a good accuracy as the point at which the tangential velocity of the stream equals that of the ring. An even more exact expression can be obtained if the presence of Coriolis forces in the system is taken into account. In this case, the velocity distribution in the ring is described by the law

$$v_\phi^{\text{ring}} = \sqrt{\Omega^2 r^2 + v_K^2} - \Omega r\,.$$

Therefore, the condition $v_\phi^{\text{ring}}(R_h) = v_\phi^{\text{stream}}(R_h)$ gives the dependence $R_h(q)$ coinciding with the theoretical one in [35]. The dependence of R_h on q is illustrated in Fig. 2c.

The radius dependence of the matter angular velocity, $\Omega_K = v_K/r$, implies differential rotation of the gas in the ring, i.e., nonzero shear stress in the gas stream. Dissipative processes decelerate the rotation of gas particles in inner orbits and accelerate it in outer orbits. As a result, the angular momentum undergoes redistribution within the ring, which spreads out into an accretion disk.

Examination of physical processes in accretion disks described in many monographs and original papers (see, e.g., Refs [8, 37–46]) is a very difficult task. We do not pretend to coherently expose the theory of accretion disks and only briefly touch on the main physical phenomena inherent in them. We refer the reader for the details to a special publication on accretion disks and present here only the minimum of knowledge necessary to understand the material that follows.

The thickness of the accretion disk depends on the balance of heating and cooling. Effective cooling results in a geometrically thin disk that can be described by introducing the surface density Σ, i.e., the mass of matter per unit surface,

$$\Sigma = 2\int_0^H \rho\,\mathrm{d}z\,,$$

where H is the disk half-thickness. Variation of the surface density Σ with time determines the dynamics of the accretion disk [38, 40, 44, 45, 47].

Dissipative processes in the disk are responsible for the radial motion of matter toward the accretor with a velocity v_{rad}. Equations describing thin disk dynamics are usually derived from the complete system of 3D[2] gasdynamic equations by integration over disk thickness under the assumption that the disk is Keplerian (i.e., $v_\phi = v_K = r\Omega_K = \sqrt{GM_2/r}$) and v_{rad} is independent of z. It follows from the mass conservation law at a radius r that

$$r\,\frac{\partial\Sigma}{\partial t} + \frac{\partial}{\partial r}\,rv_{\text{rad}}\Sigma = 0\,. \tag{2}$$

It follows from the angular momentum conservation law that

$$r\,\frac{\partial}{\partial t}\,\Sigma r^2\Omega + \frac{\partial}{\partial r}\,rv_{\text{rad}}\Sigma r^2\Omega = \mathcal{G}\,, \tag{3}$$

where

$$\mathcal{G} = \frac{1}{2\pi}\,\frac{\partial F}{\partial r}$$

and F is the viscous force moment at the radius r,

$$F = 2\pi r\,\nu\Sigma r\,\frac{\partial\Omega}{\partial r}\,r\,.$$

Here, ν is the kinematic viscosity coefficient and $r\,\partial\Omega/\partial r$ is the shear stress.

Combining (2) and (3) yields equations describing the time evolution of the surface density Σ and the radial velocity v_{rad} for a Keplerian disk:

$$\frac{\partial\Sigma}{\partial t} = \frac{3}{r}\,\frac{\partial}{\partial r}\left[\sqrt{r}\,\frac{\partial}{\partial r}\,(\nu\Sigma\sqrt{r})\right], \tag{4}$$

$$v_{\text{rad}} = -\frac{3}{\Sigma\sqrt{r}}\,\frac{\partial}{\partial r}\,\nu\Sigma\sqrt{r}\,. \tag{5}$$

An important property of Eqn (4) is its diffusion type, meaning that the disk surface density may change only on the viscous time scale

$$t_\nu(r) \sim \frac{r^2}{\nu}\,, \tag{6}$$

or, in other words, the radial velocity of mass transfer through the disk is proportional to $\sim r/t_\nu \sim \nu/r$.

From the physical standpoint, the radial mass flow in the disk is described by the diffusion equation rather than the equation of motion because the gas cannot accrete until the excess of its angular momentum is eliminated. Viscosity causes redistribution of the angular momentum inside the disk, withdrawing it from inner disk regions to outer ones; this ensures accretion of the inner parts.

We use Eqn(4) and calculate the time evolution of surface density in the case of a constant viscosity ν. Initially, the surface density distribution is described as a perturbation (δ-function) at the disk half-radius. Time evolution for four instants $t = 1\times10^{-3}t_0$, $t = 2\times10^{-3}t_0$, $t = 4\times10^{-3}t_0$, and

[2] Two-dimensional equations obtained using this approach are not totally correct [see comparison of the sets of equations (10) and (11) below].

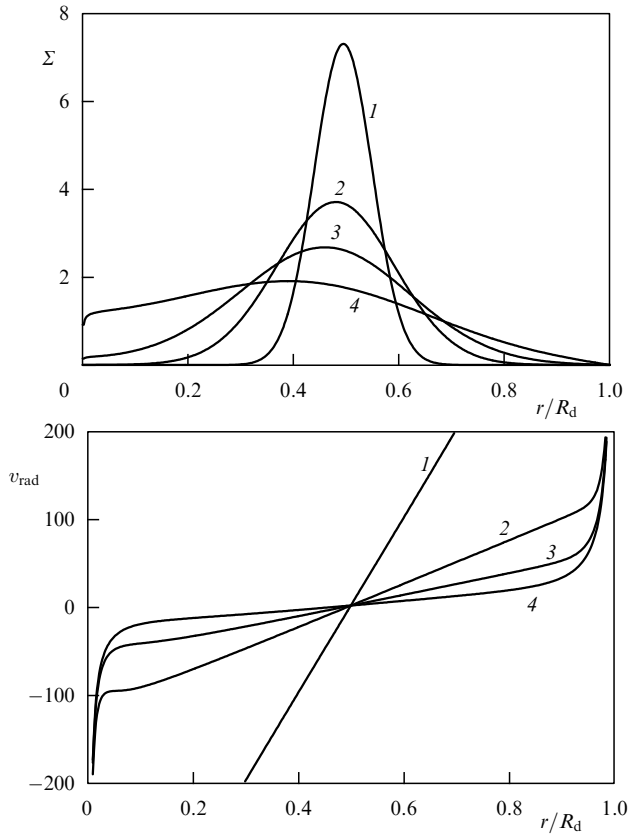

Figure 3. Time evolution of a gaseous ring under the effect of viscosity. The figure shows distribution of the surface density Σ and the radial velocity of spreading $v_{\rm rad}$ from a radius r for four time instants (see text for details).

$t = 9 \times 10^{-3} t_0$, is presented in Fig. 3 (curves *1–4*, respectively). The time scale was chosen as $t_0 = R_{\rm d}^2/\nu$ based on the assumed viscosity value νv and the disk radius $R_{\rm d}$. Figure 3 also shows $v_{\rm rad}$ (in units of $\nu/R_{\rm d}$) for the same instants. The results of calculations indicate that the bulk of ring matter moves to the inside, losing energy and angular momentum. Only its small portion streams to the outside and acquires angular momentum. As a result, the starting ring spreads out into a disk as expected.

The fate of the disk outer layers depends on the fact that a stationary disk has to permanently eliminate the excessive angular momentum. Given a large disk, the tidal forces from the companion star limit its further growth and transfer the excess of its angular momentum into the orbital momentum of the binary system. Moreover, an excess of angular momentum can be transferred from the outer disk edge to the gas of the circumbinary envelope that afterwards escapes from the system (matter decretion). This mechanism appears to coexist with other modes of elimination of the excessive angular momentum from disk matter (e.g., magnetic wind, spiral shock waves) that should also be taken into consideration in the analysis of accretion disks.

The disk structure in the direction normal to the disk plane (along the z axis) is determined by the balance between the vertical constituent of the pressure gradient and the z component of the stellar gravity force. Under the assumption of a negligibly small disk mass,

$$\frac{\partial p}{\partial z} = \rho \, \frac{\partial}{\partial z}\left(\frac{GM_2}{\sqrt{r^2 + z^2}}\right). \tag{7}$$

For a thin disk, $z \ll r$; therefore, Eqn (7) can be reduced

$$\frac{\partial p}{\partial z} = \frac{GM_2 \rho z}{r^3}. \tag{8}$$

For the purpose of assessment, it is convenient to use a simplified equation derived from (8) under the assumption that

$$\frac{\partial p}{\partial z} \approx \frac{p_0}{H}, \qquad z \approx H, \qquad c_{\rm s} \approx \sqrt{\frac{p_0}{\rho_0}},$$

where the subscript 0 corresponds to the values taken on the equatorial plane. Hence, the resulting equation for the disk half-thickness H becomes

$$H \simeq \sqrt{\frac{c_{\rm s}^2}{GM_2/r^3}} = \frac{c_{\rm s}}{v_{\rm K}}\, r, \tag{9}$$

where $c_{\rm s}$ is the speed of sound. In real astrophysical disks, a gas particle undergoes the action of additional forces (such as the pressure gradient), in addition to that of the centrifugal force and gravity forces. This means that the rotation law in such disks may differ from the Keplerian one. In this case, the gas particle dynamics in the disk are described by the momentum conservation equation in the radial direction and by the hydrostatic equilibrium equation in the vertical direction. The corresponding set of equations can be written in the following form under the assumption of axial symmetry and the polytropic gas state equation:

$$\begin{aligned} &\frac{\partial v_{\rm rad}}{\partial t} + v_{\rm rad}\,\frac{\partial v_{\rm rad}}{\partial r} + \frac{1}{\rho}\,\frac{\partial p}{\partial r} = -\frac{\partial \Phi}{\partial r} + \frac{v_\phi^2}{r}, \\ &\frac{1}{\rho}\,\frac{\partial p}{\partial z} = -\frac{\partial \Phi}{\partial z}, \\ &p = K\rho^{\,1+1/n}. \end{aligned} \tag{10}$$

Thin disks are usually described based on the standard set of 'flat' equations averaged over z:

$$\begin{aligned} &\frac{\partial v_{\rm rad}}{\partial t} + v_{\rm rad}\,\frac{\partial v_{\rm rad}}{\partial r} + \frac{1}{\Sigma}\,\frac{\partial \Pi}{\partial r} = -\frac{\partial \Phi_0}{\partial r} + \frac{v_\phi^2}{r} \\ &\Pi = K_1 \Sigma^{\,1+1/n_1}, \end{aligned} \tag{11}$$

where, as usual, Σ is the surface density,

$$\Pi = 2\int_0^H p\,{\rm d}z$$

is the 'flat' pressure, and K and K_1 are constants. In system (11), Φ_0 stands for the first term in the expansion of the potential Φ with respect to z in the vicinity of the equatorial plane (the prime denotes differentiation with respect to z):

$$\Phi = \Phi_0(r) + \frac{1}{2}\,\Phi_0''(r)\, z^2 + \ldots,$$

and n_1 is the 'flat' polytropic index.

However, the sets of equations (10) and (11) are not equivalent in the general case [48, 49]. Indeed, it follows from the second equation in (10) that the function

$$\chi = \Phi + \int \frac{{\rm d}p}{\rho}$$

depends on r alone, which allows writing the density ρ as

$$\rho = \left(\frac{\chi(r) - \Phi_0(r) - (1/2)\Phi_0''(r)\, z^2}{K(n+1)}\right)^n .$$

Integrating the expression for the density with respect to z from $-H$ to H and taking into account that the disk half-thickness is defined in this case as $H = \sqrt{2(\chi - \Phi_0)/\Phi_0''}$, we obtain the relation between χ and Σ:

$$\chi(r) = \Phi_0(r) + C(r)\, \Sigma^{2/(2n+1)} ,$$

where

$$C(R) \sim \left[\Phi_0''(R)\right]^{1/(2n+1)} .$$

To obtain a 'flat' equation for momentum in the radial direction with correct averaging, it is necessary to differentiate $\chi(r)$ with respect to r. Differentiation yields

$$\frac{\partial v_{\rm rad}}{\partial t} + v_{\rm rad}\, \frac{\partial v_{\rm rad}}{\partial r} + \frac{2}{2n+1}\, C(r)\Sigma^{-(2n-1)/(2n+1)} + \frac{{\rm d}C}{{\rm d}r}\, \Sigma^{2/(2n+1)} = -\frac{\partial \Phi_0}{\partial r} + \frac{v_\phi^2}{r} . \quad (12)$$

This equation is different from its counterpart in (11), which can be written as

$$\frac{\partial v_{\rm rad}}{\partial t} + v_{\rm rad}\, \frac{\partial v_{\rm rad}}{\partial r} + K_1\, \frac{n_1+1}{n_1}\, \Sigma^{-(n_1-1)/n_1} = -\frac{\partial \Phi_0}{\partial r} + \frac{v_\phi^2}{r} . \quad (13)$$

Thus, Eqn (12) differs from the standard Eqn (13) not only in that it contains an additional term with ${\rm d}C/{\rm d}r$ but also in that it has different powers of Σ in the term describing the pressure gradient if identical polytropic indices $n_1 = n$ are used in both full and 'flat' models. This difference disappears only in the isothermic case corresponding to $n \to \infty$, where ${\rm d}C/{\rm d}r \to 0$.[3] In the above axisymmetric polytropic case, the disk can be described in the 'flat' variant with modified momentum equation (12).

Modified flat equations in the nonaxisymmetric polytropic case (49) are extremely difficult to analyze. That is why complete 3D equations are preferred to describe accretion disks in an external gravitational field. As regards the more general case in which disk matter is not described by a barotropic equation of state[4] but has a form $p = p(\rho, \varepsilon)$, the possibility of obtaining the correct closed system of 'flat' equations remains open [49]. We emphasize that the importance of the three-dimensional approach stems from the fact that an averaged 'flat' consideration of thick discs is impossible in principle.

Dissipative viscous processes play a key role in the physics of accretion disks. We consider an equilibrium gaseous configuration near the gravitating center. Dissipative processes cause redistribution of the angular momentum and thereby induce the radial motion of matter. If the angular momentum is either lost by or withdrawn from the system, matter starts moving toward the gravitating center; this sooner or later leads to accretion. It is therefore possible to state that only the presence of dissipative processes turns the initial equilibrium gaseous configuration into an accretion disk.

The source of viscosity in differentially rotating gaseous disks remains to be discovered; it accounts for the popularity of the phenomenological theory of the α-disk. This theory is based on the parameterization of the kinematic viscosity coefficient proposed in Refs [41, 42] in the form

$$\nu = \alpha c_{\rm s} H , \quad (14)$$

where α is a dimensionless parameter.

The development of a correct accretion disk model requires knowledge of the viscosity ν or, which is equivalent, the coefficient α. Some data on the range of possible α values in accretion disks are available from observations. According to sufficiently reliable experimental estimates, $\alpha \sim 0.01-1$ (see, e.g., Refs [50–53]). Evidently, these values are much greater than the corresponding molecular viscosity ($\alpha \sim 10^{-11}$). It remains to find the physical mechanisms responsible for such a high viscosity in accretion disks.

2.2 Temperature of accretion disks

The aim of the present section is to estimate the possible temperature range of accretion disks for different accretion rates $\dot{\mathfrak{M}}$, i.e., to derive the dependence $T(\dot{\mathfrak{M}})$.

2.2.1 Basic equations. As shown in Section 2.1, the vertical structure of an accretion disk depends on the equilibrium between the vertical component of the gravity force and the pressure gradient (vertical). It is, in turn, determined by the balance of gas heating and cooling processes. The process of heating is associated with viscous dissipation of kinetic energy; also, it is related to volumetric radiative heating caused by emission from the central object. The cooling process is underlain by a few mechanisms: volumetric radiation cooling, radiative thermal conductivity, and convection. Assuming that the advective terms and terms related to adiabatic heating/cooling are small, we can write the steady-state energy equation

$$Q^+ - Q^- = 0 \quad (15)$$

as follows:

(1) In an optically thin case where Q^+ is determined by volumetric radiative heating and viscous heating, and Q^- is given by volumetric radiative cooling,

$$Q^+_{\rm visc}(\rho, T) + n^2\left[\Gamma(T, T_{\rm wd}) - \Lambda(T)\right] = 0 . \quad (15a)$$

Here, $\Gamma(T, T_{\rm wd})$ is a function of the radiative heating depending on the gas temperature T and the temperature of the central object (white dwarf) $T_{\rm wd}$, $\Lambda(T)$ is the function of radiative cooling, and $Q^+_{\rm visc}(\rho, T)$ is the viscous heating.

(2) In an optically thick case where Q^+ is determined by viscous heating and Q^- by radiative thermal conductivity,[5] and convection occurs in the vertical direction,

$$Q^+_{\rm visc}(\rho, T) - \frac{\partial F_{\rm rad}}{\partial z} - \frac{\partial F_{\rm conv}}{\partial z} = 0 . \quad (15b)$$

Here, $F_{\rm rad}$ and $F_{\rm conv}$ are the radiative and convective energy fluxes.

[3] It is worthy of note that a similar consideration of a self-gravitating disk demonstrates that the standard 'flat' equations are also valid only in one case, at $n = 1$ [49].

[4] Exemplified by the equation of state $p = (\gamma - 1)\rho\varepsilon$ for an ideal gas.

[5] Molecular heat conductivity is disregarded because it is low compared with the radiative one.

To find the functions entering Eqns (15a) and (15b), we need the continuity equation

$$-\dot{\mathfrak{M}} = 2\pi \int r\rho v_r \, dz = \text{const}\,, \tag{16}$$

the angular momentum balance equation $\lambda \equiv r^2\Omega_K$ in the radial direction

$$\frac{\partial}{\partial r}(r\rho v_r \lambda) = \frac{\partial}{\partial r}\left(v\rho r^2 \frac{\partial \Omega_K}{\partial r}\right), \tag{17}$$

which implies that

$$|v_r| = -v\,\frac{\partial \Omega_K}{\partial r}\,\Omega_K^{-1} r^{-1} \simeq v r^{-1}\,, \tag{18}$$

and the viscous heating equation

$$Q^+_{visc} = \rho v \left(r\,\frac{\partial \Omega_K}{\partial r}\right)^2. \tag{19}$$

Here, $\Omega_K = \sqrt{GM/r^3}$ is the angular rotation velocity of the Keplerian disk, M is the mass of the central object, ρ is the matter density, v_r is the radial velocity, and v is the kinematic viscosity coefficient. As noted above, molecular viscosity does not ensure the necessary dissipation. Therefore, it is usually assumed that dissipative processes are associated either with turbulent viscosity or with magnetic viscosity.

The vertical pressure gradient can be found using the equation for hydrostatic equilibrium in the vertical direction:

$$\frac{1}{\rho}\frac{\partial P}{\partial z} = \frac{\partial}{\partial z}\left(\frac{GM}{\sqrt{r^2+z^2}}\right) \simeq -\Omega_K^2 z\,, \tag{20}$$

and the equation of state for an ideal gas with emission

$$P = \rho \mathcal{R} T + \frac{1}{3}\,aT^4\,.$$

Here, as usual, P is the pressure, T is the temperature, $\mathcal{R}$ is the gas constant, and a is the radiation constant. All the equations are written in the cylindrical coordinate system (r, z).

2.2.2 Solution method. To find the dependence $T(\dot{\mathfrak{M}})$, Eqns (16) and (18) are needed, along with the expressions for the viscosity coefficient v. We use the expression for v proposed in Refs [41, 42]: $v = \alpha c_s H$, where H is the disk half-thickness and $c_s \simeq \sqrt{\mathcal{R}T + (1/3)aT^4/\rho}$. With the dependence of density on z neglected and with the value of ρ averaged over the height (hereinafter denoted as $\bar{\rho}$) used, integration of Eqn (20) gives the following expression for the disk half-thickness H:

$$H = c_s \Omega_K^{-1}\,.$$

The value of c_s can be found from the temperature in the disk equatorial plane, $z = 0$. This procedure is sufficiently correct in view of the uncertainty in the parameter α. It results in the equation relating $\dot{\mathfrak{M}}$, $T\big|_{z=0}$, and ρ at given r and α:

$$\dot{\mathfrak{M}} = 2\pi\alpha\Omega_K^{-2}\rho c_s^3 = 2\pi\alpha\Omega_K^{-2}\left(\mathcal{R}T\rho^{2/3} + \frac{1}{3}\,aT^4\rho^{-1/3}\right)^{3/2}. \tag{21}$$

Equation (21) reduces to a cubic equation for $\rho^{1/3}$ and has two solution variants: either one negative real and two complex roots or three real roots, one of which is negative. In terms of the physical meaning of density, only positive real roots are meaningful. These roots exist under the condition that

$$\dot{\mathfrak{M}} > \frac{\sqrt{3}\pi\sqrt{\mathcal{R}}\,a\alpha T^{9/2}}{\Omega_K^2}\,, \tag{22}$$

yielding the minimal accretion rate at given T, r, and α. Condition (22) was derived using the equation of state with the radiation pressure taken into account.

This estimate can be written as

$$T < 7\times 10^5 \left(\frac{r}{R_{wd}}\right)^{-2/3}\left(\frac{\dot{\mathfrak{M}}}{10^{-9} M_\odot\ \text{yr}^{-1}}\right)^{2/9}\left(\frac{\alpha}{0.1}\right)^{-2/9}[\text{K}]\,,$$

where $R_{wd} = 10^9$ cm is the radius of the accretor (white dwarf).

We consider condition (22) for the outer regions of an accretion disk, assuming $r = A/5$, where A is the distance between components of the binary system and $A = 1.42 R_\odot$, as in IP Peg; then,

$$\dot{\mathfrak{M}} > 10^{-9}\left(\frac{T}{10^5\ \text{K}}\right)^{9/2}\left(\frac{\alpha}{0.1}\right)[M_\odot\ \text{yr}^{-1}]\,. \tag{23}$$

With condition (22) satisfied, the roots of Eqn (21) relating ρ, T, and $\dot{\mathfrak{M}}$ at given r and α can be written as

$$\rho = (\mathcal{R}T)^{-3/4}\left(\frac{\dot{\mathfrak{M}}\Omega_K^2}{2\pi\alpha}\right)\sin^3\left[\frac{1}{3}\arcsin\left(\sqrt{\mathcal{R}}\,aT^{9/2}\,\frac{2\pi\alpha}{\dot{\mathfrak{M}}\Omega_K^2}\right)\right],$$

$$\rho = (\mathcal{R}T)^{-3/4}\left(\frac{\dot{\mathfrak{M}}\Omega_K^2}{2\pi\alpha}\right) \times \cos^3\left[\frac{1}{3}\arcsin\left(\sqrt{\mathcal{R}}\,aT^{9/2}\,\frac{2\pi\alpha}{\dot{\mathfrak{M}}\Omega_K^2}\right) + \frac{\pi}{6}\right],$$

where numerical factors $\sqrt{3}/2 \simeq 1$ are omitted for simplicity. The first root in Eqn (21) corresponds to the so-called radiation-pressure-dominated disks: $\beta = (1/3)aT^4/\rho\mathcal{R}T > 1$, and the second one corresponds to those dominated by gaseous pressure: $\beta < 1$.

These formulas describe two branches of the two-parameter dependence $\rho(\dot{\mathfrak{M}}, T)$. For our purposes, i.e., for calculating the dependence $T(\dot{\mathfrak{M}})$, an additional equation is needed, namely the thermal balance equation (15). It follows from Section 2.2.1 that Eqn (15) has different forms depending on the optical thickness of the disk; hence, the necessity to calculate the optical density.

2.2.3 Optical thickness. The optical thickness τ is the product of the absorption coefficient κ_{abs}, the density, and the geometric thickness of the layer: $\tau = \kappa_{abs}\,\rho l$. The key parameter for disk accretion is the ratio of the geometric thickness of the layer at which the value of $\tau = 1$ is achieved to the disk half-thickness: $l^{\tau=1}/H$. Simple transformation yields

$$\frac{l^{\tau=1}}{H} = \frac{2\pi\alpha}{\kappa_{abs}\dot{\mathfrak{M}}}\,c_s^2\Omega_K^{-1}\,. \tag{24}$$

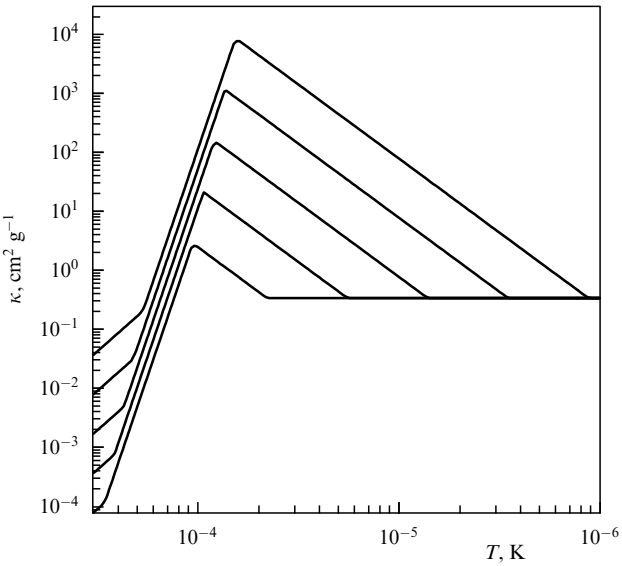

Figure 4. The dependence $\kappa_{\rm abs}(T)$ for the values $n = 10^{18}$ cm^{-3}, 10^{17} cm^{-3}, 10^{16} cm^{-3}, 10^{15} cm^{-3}, and 10^{14} cm^{-3} (from top down) [55].

The absorption coefficient $\kappa_{\rm abs}$ shows a complex dependence on T and ρ and on the degree of ionization, chemical composition, etc. In this review, a simple approximation for $\kappa_{\rm abs}(T,\rho)$ is accepted [14, 54, 55]:

$$\kappa_{\rm abs}(T,\rho) = \begin{cases} \kappa_1\,\rho^{2/3}T^3\,, & \kappa_1 = 10^{-8}\,, \\ \kappa_2\,\rho^{1/3}T^{10}\,, & \kappa_2 = 10^{-36}\,, \\ \kappa_3\,\rho T^{-5/2}\,, & \kappa_3 = 1.5\times 10^{20}\,, \\ \kappa_4\,, & \kappa_4 = 0.348\,. \end{cases}$$

According to Ref. [55], these four subregions correspond to scattering on molecular and atomic hydrogen, to free – free and free – bound transitions, and to Thompson scattering. The boundaries of the subregions at which transitions from one expression to another occur are given by the matching condition for the $\kappa_{\rm abs}$ values computed from these expressions. The plots of $\kappa_{\rm abs}$ versus T and ρ are presented in Fig. 4. It shows regions with $\mathrm{d}\kappa_{\rm abs}/\mathrm{d}T > 0$, where a thermal instability develops when the dependence between the surface density and the disk temperature follows an S-curve on the $(\Sigma, T_{\rm eff})$ plane. Thermal instability is frequently used to explain outbursts of dwarf novae (see, e.g., Refs [52, 56]). It is evident, however, that this approach holds only for sufficiently cold disks.

We return to Eqn (21), set $\alpha = 0.1$ and $r = A/5$, and consider disks dominated by gaseous pressure for which $\beta = (1/3)aT^4/\rho\mathcal{R}T < 1$. Figure 5a shows a shaded region in the $(T, \dot{\mathfrak{M}})$ plane corresponding to all possible solutions for the disks under consideration. The dashed line corresponds to condition (23), under which Eqn (21) can be solved. Solutions are absent in the region below this line. The solid line is the boundary between optically thick and thin solutions: horizontal and vertical hatchings show regions of optically thick and thin disks, respectively. A similar analysis for disks dominated by radiation pressure ($\beta > 1$) is presented in Fig. 5b.

It follows from Fig. 5a that most gaseous pressure-dominated disks are optically thick at real values $\dot{\mathfrak{M}} \in [10^{-12}, 10^{-7}]\ M_\odot$ yr^{-1}, although solutions corresponding to optically thin cold disks are conceivable at small $\dot{\mathfrak{M}}$. Figure 5b shows that the majority of the disks dominated by radiation pressure are optically thin, while thick hot disks can exist only at large $\dot{\mathfrak{M}}$.

2.2.4 Optically thick disks. In Section 2.2.2, Eqn (21) relating $\dot{\mathfrak{M}}$, T, and ρ at given r and α was derived. Additionally using thermal balance equation (15) allows reducing the number of unknowns and finding the sought relation between $\dot{\mathfrak{M}}$ and T.

The vertical distribution of temperature in optically thick disks is described by the equation for radiative thermal conductivity with a source due to viscous heating (15b). This

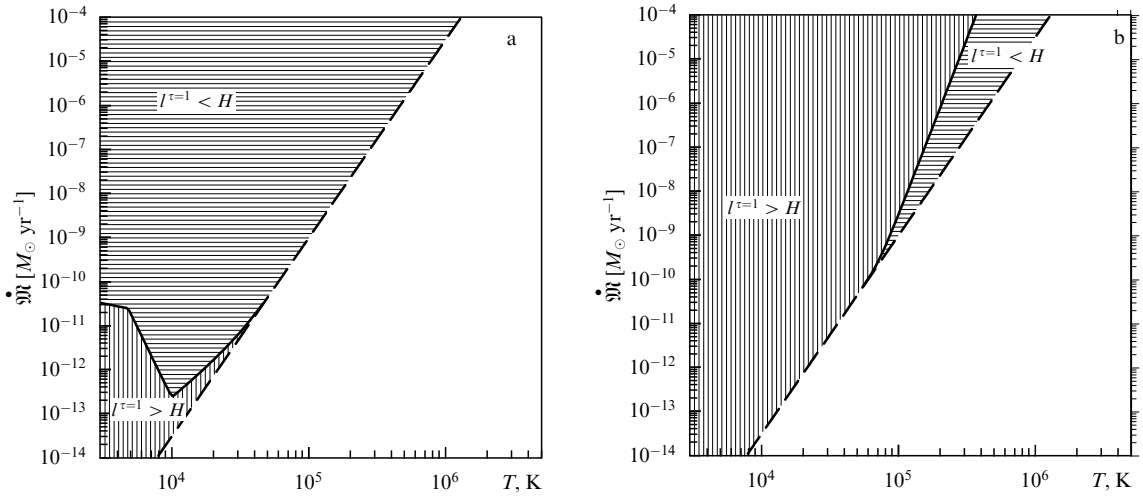

Figure 5. (a) Solutions of Eqn (21) for disks dominated by gaseous pressure on the plane $(T, \dot{\mathfrak{M}})$ for $\alpha = 0.1$ and $r = A/5$. Horizontal and vertical hatchings show optically thick and thin disks, respectively. The solid line is the boundary between these regions. The dashed line corresponds to condition (23) under which the solution of Eqn (21) is possible. Solutions are absent in the region below this line. (b) The same for solutions of Eqn (21) for disks dominated by radiation pressure.

equation can be written as

$$\frac{\partial e}{\partial t} = \frac{\partial}{\partial z}\left[\frac{1}{\kappa_{\rm abs}\,\rho}\,\frac{\partial}{\partial z}\left(\frac{1}{3}\,acT^4\right)\right] + \rho\alpha c_{\rm s}^2\Omega_{\rm K}\,, \qquad (25)$$

where e is the specific internal energy and c is the speed of light. Equation (25) can be solved if boundary conditions are known. Due to the problem symmetry, the temperature derivative in the equatorial plane vanishes, $T'|_{z=0} = 0$. The temperature at the upper boundary of the disk is found from the condition $\Gamma(T_*, T_{\rm wd}) = \Lambda(T_*)$. The functions $\Gamma(T, T_{\rm wd})$ and $\Lambda(T)$ have an intricate form, but they are well known (see, e.g., Refs [57–59]). The temperature determined from the equality of these functions is $T(H) = T_* = 13{,}600$ K (the temperature of the central object, a white dwarf, is $T_{\rm wd} = 70{,}000$ K).

The solution of Eqn (25) comes to the steady-state regime when the characteristic thermal conductivity time

$$t_{\rm diff} \simeq \frac{\mathcal{R}\kappa_{\rm abs}\,\rho^2 H^2}{acT^3}$$

becomes comparable with the viscous heating time

$$t_{\rm heat} \simeq \frac{\mathcal{R}T}{\alpha c_{\rm s}^2\Omega_{\rm K}} \simeq \alpha^{-1}\Omega_{\rm K}^{-1}\,.$$

We note that Eqn (25) can be integrated analytically in the stationary case. We set $U = T^4$, $U_* = T_*^4$, and $U_0 = U|_{z=0}$ and again assume that ρ is independent of z; then,

$$\frac{\rm d}{{\rm d}z}\left[\frac{1}{\kappa_{\rm abs}\,\rho}\,\frac{\rm d}{{\rm d}z}\left(\frac{ac}{3}\,U\right)\right] = -\rho\alpha c_{\rm s}^2\Omega_{\rm K}\,.$$

Integration over z leads to

$$\frac{1}{\kappa_{\rm abs}\,\rho}\,\frac{\rm d}{{\rm d}z}\left(\frac{ac}{3}U\right) = -\rho\alpha c_{\rm s}^2\Omega_{\rm K} z\,,$$

and the integration constant vanishes because $U'|_{z=0} = 0$. For simplicity, we rewrite the last equation as

$$\frac{1}{\kappa_{\rm abs}}\,\frac{{\rm d}U}{{\rm d}z} \equiv \frac{{\rm d}B}{{\rm d}z} = -\frac{3}{ac}\,\rho^2\alpha c_{\rm s}^2\Omega_{\rm K} z\,,$$

where the function $B(U)$ found from the differential equation

$$\frac{{\rm d}B}{{\rm d}U} = \frac{1}{\kappa_{\rm abs}(U,\rho)}$$

can be written in analytic form for a fixed ρ. Integration of the last equation over z yields

$$B(U) = B(U_*) + \frac{3}{2ac}\,\rho^2\alpha c_{\rm s}^2\Omega_{\rm K}(H^2 - z^2)\,,$$

or for $z = 0$,

$$B(U_0) = B(U_*) + \frac{3}{2ac}\,\rho^2\alpha c_{\rm s}^2\Omega_{\rm K} H^2\,.$$

Using the expressions

$$c_{\rm s}^2 = \left(\mathcal{R}U_0^{1/4} + \frac{1}{3}\,\frac{aU_0}{\rho}\right),$$

$$H^2 = \left(\mathcal{R}U_0^{1/4} + \frac{1}{3}\,\frac{aU_0}{\rho}\right)\Omega_{\rm K}^{-2}$$

gives an algebraic equation for U_0:

$$B(U_0) = B(U_*) + \frac{3}{2ac}\,\rho^2\alpha\Omega_{\rm K}^{-1}\left(\mathcal{R}U_0^{1/4} + \frac{1}{3}\,\frac{aU_0}{\rho}\right)^2.$$

This equation implicitly defines the dependence $U_0(\rho)$, i.e., $T(\rho)$. The expression of $\dot{\mathfrak{M}}$ in terms of ρ and T gives the dependence $\dot{\mathfrak{M}}(\rho) = \dot{\mathfrak{M}}\big(T(\rho), \rho\big)$ and therefore the sought dependence $T(\dot{\mathfrak{M}})$ in parametric form. Formally, the solution was also obtained in optically thin regions, but these points were discarded on account of the above assumptions.

We consider the graphical representation of the results of the solution of this equation. Asterisks in Fig. 6a denote the dependence $T(\dot{\mathfrak{M}})$ for $\alpha = 1$ and $r = A/5$. Similarly to Fig. 5, the dashed line delimits the region of solutions of Eqn (21) from below, and the solid line separates regions of optically thin and thick disks. Figure 6b presents the solutions for $\alpha = 0.1$ and $\alpha = 0.01$, respectively, and Fig. 6d shows the dependence of the accretion rate on the disk thickness. All the disks are geometrically thin, i.e., $H \ll r$.

Radiative thermal conductivity is not the sole mechanism of the released heat transfer to optically thin regions. Convection may also play an important role under certain conditions. Neglecting radiation pressure, we can write the convective flux as [60, 61]

$$F_{\rm conv} = c_P\,\rho\left(\frac{|g|}{T}\right)^{1/2}\frac{l^2}{4}\,\big[\Delta(\nabla T)\big]^{3/2}\,,$$

$$\Delta(\nabla T) = -\frac{T}{c_P}\,\frac{\partial S}{\partial z}\,,$$

where c_P is the thermal capacity at a constant pressure, $S = \mathcal{R}\ln(T^{3/2}/\rho)$ is the specific entropy, $g = -\Omega_{\rm K}^2 z$ is the acceleration of gravity, and l is the mixing length assumed to be given by $l = \alpha H$. To determine the vertical temperature distribution with the convection taken into account, we must solve the equation

$$\frac{\partial e}{\partial t} = \frac{\partial}{\partial z}\left[\frac{1}{\kappa_{\rm abs}\,\rho}\,\frac{\partial}{\partial z}\left(\frac{1}{3}\,acT^4\right)\right] - \frac{\partial F_{\rm conv}}{\partial z} + \rho\alpha c_{\rm s}^2\Omega_{\rm K} \qquad (26)$$

with the same boundary conditions as for Eqn (25). Equation (26) does not allow a simple analytic solution and was solved numerically by the relaxation method. The solution obtained is shown by squares in Fig. 6a–d. It appears that convection is essential only for $\alpha \simeq 1$.

Summarizing the results of the above analysis, it may be stated that an optically thick disk at small $\dot{\mathfrak{M}}$ has the constant temperature $T = T_* = 13{,}600$ K; at greater $\dot{\mathfrak{M}}$, the disk temperature increases as $T \propto \dot{\mathfrak{M}}^{1/3}$. This means that for realistic parameters of accretion disks in CBS $\dot{\mathfrak{M}} \simeq (10^{-12} - 10^{-7})M_\odot$ yr^{-1} and $\alpha \simeq 10^{-1} - 10^{-2}$, the gas temperature in the outer regions of the disk ($r \simeq A/5 - A/10$) ranges from $\sim 10^4$ K to $\sim 10^6$ K.

In solving Eqn (25) with different r, it is possible to compute dependences $T(r)$ and $\rho(r)$. Analysis of the obtained results shows that $T \propto r^{-0.8}$, $\rho \propto r^{-1.8}$, in perfect agreement with the result $T \propto r^{-3/4}$ in [42].

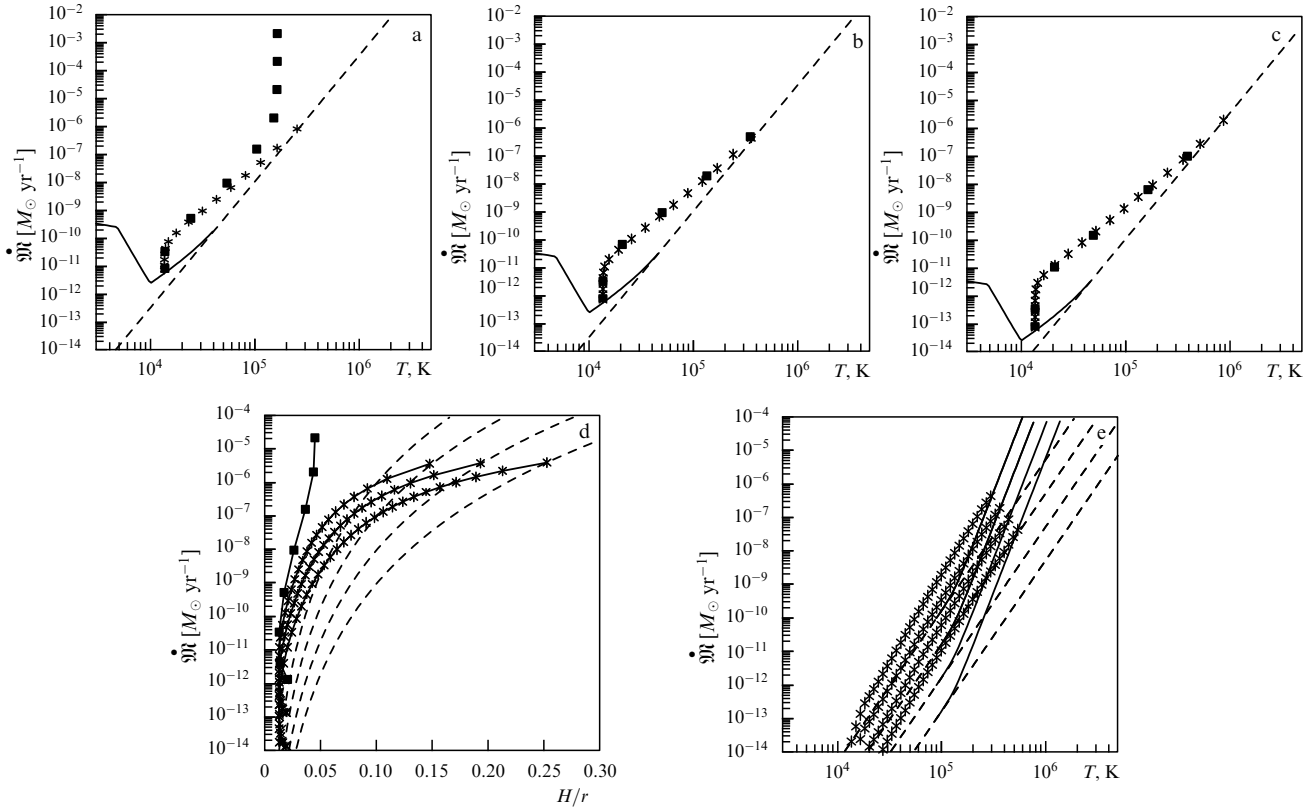

Figure 6. (a) Solutions of Eqn (25) for an optically thick disk (asterisks) at $\alpha = 1$ and $r = A/5$ and solutions of Eqn (26) with convection taken into account (squares); the dashed line delimits the region of solutions of Eqn (21) from below, the solid line separates regions of optically thin and thick disks. (b) The same at $\alpha = 0.1$. (c) The same at $\alpha = 0.01$. (d) Disks dominated by gaseous pressure. Solid lines show possible states of the disk on the $(H/r, \dot{\mathfrak{M}})$ plane for $r = A/5$. Curves marked by asterisks are solutions of Eqn (25) with radiative thermal conductivity and viscous heating for $\alpha = 0.1$, 10^{-2}, and 10^{-3} (from top down). The curve marked by squares is the solution of Eqn (26) with radiative thermal conductivity and viscous heating for $\alpha = 1$. The dashed lines delimit regions of solutions of Eqn (21) from below for $\alpha = 1$, 0.1, 10^{-2}, and 10^{-3} (from top down). (e) Solutions for an optically thin disk (asterisks) for $\alpha = 1$, 0.1, 10^{-2}, and 10^{-3} (from top down) and $r = A/20$. The dashed lines delimit the region of solutions of Eqn (21) from below, the solid lines separate regions of optically thin and thick disks.

2.2.5 Optically thin disks. The temperature of optically thin disks is a function of the balance between the radiative heating $\Gamma(T, T_{\rm wd})$ and viscous heating (19) on the one hand, and the radiative cooling $\Lambda(T)$ on the other hand.

Thermal balance equation (15a), which can be written in the form

$$\rho\alpha c_{\rm s}^2\Omega_{\rm K} + \rho^2 m_{\rm p}^2\big(\Gamma(T, T_{\rm wd}) - \Lambda(T)\big) = 0$$

reduces to a quadratic equation for ρ:

$$\alpha\left(\rho\mathcal{R}T + \frac{1}{3}\,aT^4\right)\Omega_{\rm K} + \rho^2 m_{\rm p}^{-2}\big(\Gamma(T, T_{\rm wd}) - \Lambda(T)\big) = 0\,.$$

The solution of this equation at fixed r and α gives the dependence $\rho(T)$ and then $T(\dot{\mathfrak{M}})$. Formally, the solution was also obtained in optically thick regions, but these points were discarded on account of the above assumptions.

The analysis in Section 2.2.3 has shown that most gaseous pressure-dominated disks are optically thick, and solutions corresponding to optically thin discs are possible only at small $\dot{\mathfrak{M}}$. In contrast, disks dominated by radiation pressure are typically optically thin. Radiation pressure dominates only in inner disk regions; for this reason, further analysis is concerned with the case $r = A/20$ (for the typical dwarf nova IP Peg, it corresponds to five radii of the accretor, the white dwarf).

The results of calculations are presented in Fig. 6e, where asterisks denote the dependences $T(\dot{\mathfrak{M}})$ for $\alpha = 1$, 0.1, 10^{-2}, and 10^{-3} (from top to bottom) and $r = A/20$. In these solutions, the disks are geometrically thick, i.e., $H \simeq r$. We note that the starting assumptions of the model restrict its applicability to geometrically thin disks; therefore, solutions for geometrically thick disks are formal.

The analysis of the principal heating and cooling processes in accretion disks of binary systems has demonstrated that the gas temperature in the outer regions of accretion disks in a CBS at realistic parameters of the disks ($\dot{\mathfrak{M}} \simeq 10^{-12} - 10^{-7}\,M_\odot$ yr^{-1} and $\alpha \simeq 10^{-1} - 10^{-2}$) ranges from 10^4 K to $\sim 10^6$ K.

3. Waves in accretion disks

A correct description of matter gasdynamics in semidetached binary systems requires solving the complete set of 3D equations. Unfortunately, solving this task was for a long time hampered by the lack of necessary computing facilities;

the flow structure was analyzed using 2D models. Pioneering studies [62–64] reported over 15 years ago opened up the possibility for numerical investigations into the gasdynamics of matter transport in the framework of more realistic 3D models. The present section reviews the results of three-dimensional numerical analysis of the flow pattern in semidetached binary systems obtained in Refs [65–72]. The total variation diminishing (TVD) method for the solution of a set of gasdynamic equations allows considering the gas flow morphology in a system despite the presence of strong density gradients. The gasdynamics of matter overflow in a semidetached system was investigated at large time intervals; this allowed elucidating specific features of the stream of the flow pattern in the equilibrated (steady-state) regime.

3.1 Shock waves

Analysis of the main heating and cooling processes in accretion disks of binary systems reported in Section 2.2. indicates that for realistic parameters of accretion disks, the gas temperature in their outer regions ranges from 10^4 K to $\sim 10^6$ K, meaning that both hot and cold accretion disks can form in these systems.

We consider the gasdynamics of matter in binary systems with hot disks. Solutions were obtained in the cases where the temperature of the outer regions of an accretion disk was $\sim (100-200) \times 10^3$ K.

Figure 7a, b gives some idea of the stream flow morphology in the systems being examined. The density and velocity vector distributions in the equatorial plane of the systems are illustrated by Fig. 7a; the velocity field is depicted in Fig. 7b as tracks of numerous particles. Figure 7a also shows the flow line (light with round dots) delimiting the accretion disk and the flow line (black with squares) passing through the shock wave at the edge of the stream. According to Ref. [37], the gasdynamics of matter flow in a semidetached binary system depends on the stream of matter from L_1, the quasielliptic accretion disk, the circumdisk halo, and the circumbinary envelope. Classification of the main elements of the overall flow pattern is based on their physical properties: (1) if gas motion is unrelated to the gravitational field of the accretor, the gas forms an circumbinary envelope filling the space between the components; (2) if the gas rotates about the accretor and thereafter mixes with the material of the stream, it does not belong to the disk but forms a circumdisk halo; (3) the accretion disk is formed from stream matter that, once

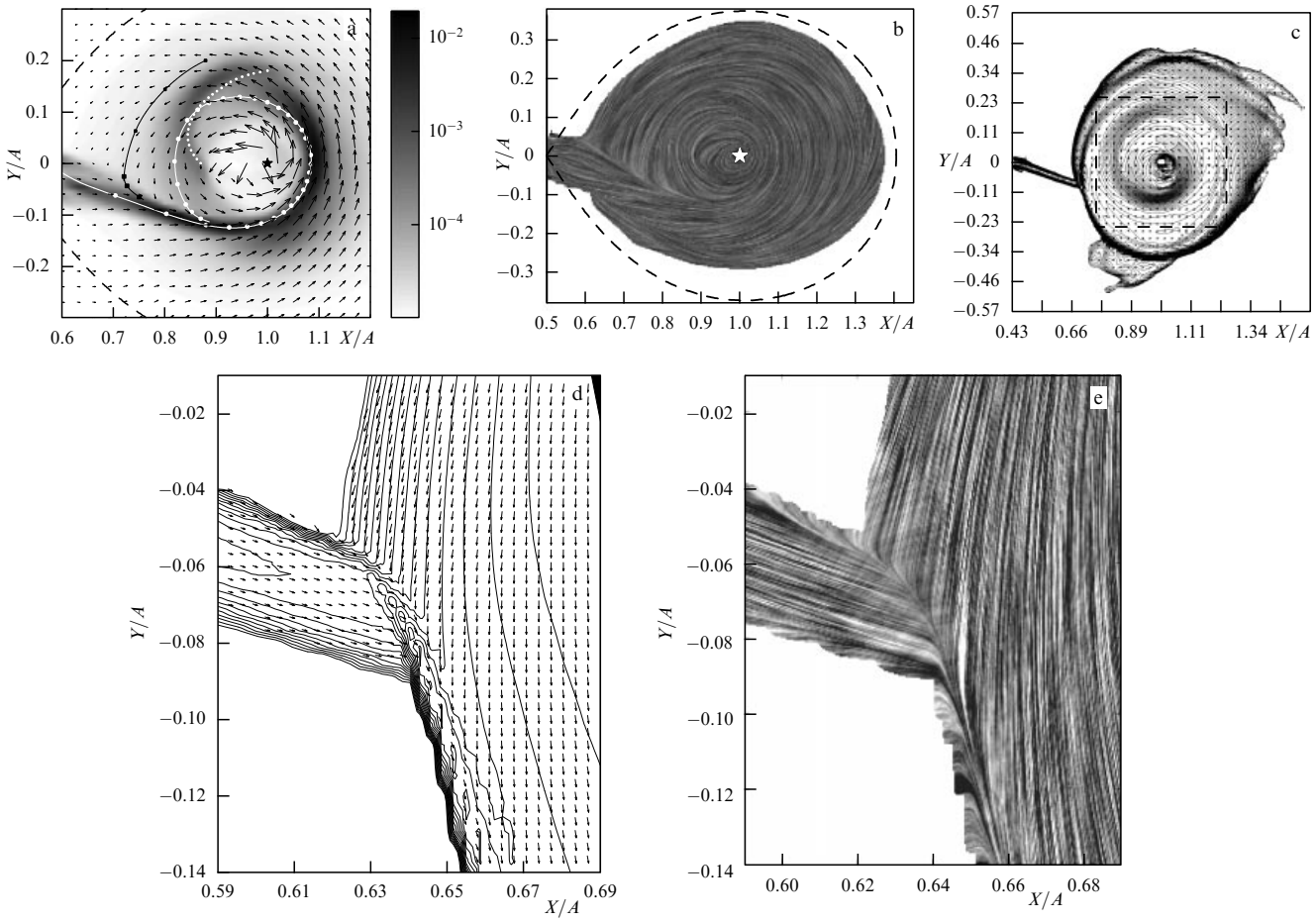

Figure 7. (a) Distribution of density and velocity vectors in the equatorial plane of a system with a hot accretion disk. Coordinates X and Y are presented in units of the distance A between the components. The asterisk marks the accretor. Dashed curves are boundaries of the Roche lobe. The light line with round dots is the flow line delimiting the accretion disk. The black line with squares is the flow line passing through the shock wave at the stream edge. Larger dots and squares on the flow lines correspond to the shock wave region. The light dotted curve is an arm of the tidal shock wave. (b) Visualization of the velocity field in the equatorial plane of the system. Coordinates X and Y are in units of the distance A between the components. The asterisk marks the accretor. The dashed curve is the boundary of the Roche lobe. (c) Distribution of density and velocity vectors in the equatorial plane of a system with a cold accretion disk. (d, e) The density and velocity vector isolines (d) and visualization of the velocity field (e) in the region of stream–halo interaction in the equatorial plane of the system for the solution with a cold accretion disk.

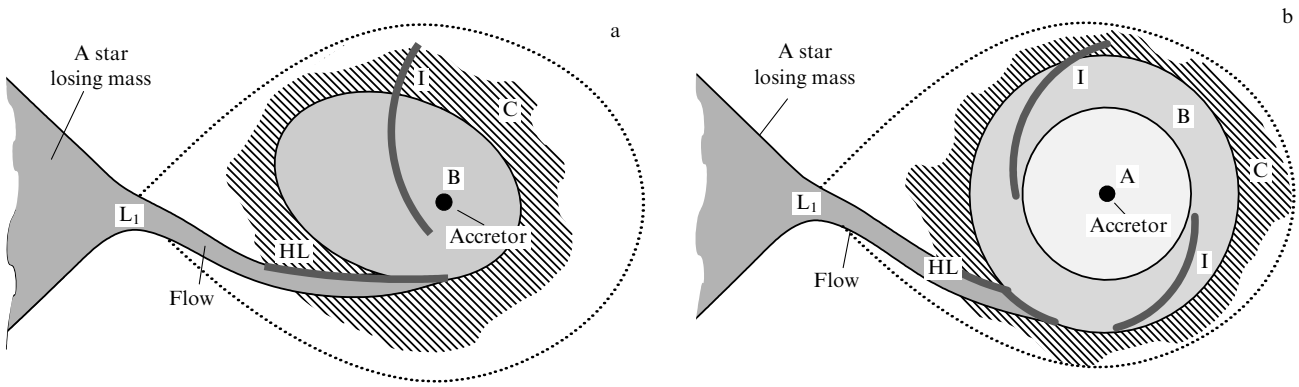

Figure 8. Schematic representation of the main features of a matter flow in semidetached binary systems at high (a) and low (b) gas temperatures. Zones A and B are accretion disks, C is the circumdisk halo, HL is the hot line, I is the arms of the spiral tidal shock wave, and L_1 is the libration point. The dotted line shows the Roche equipotential containing the inner Lagrange point.

entering the accretor's gravitational field, no longer interacts with the stream and moves toward the star, losing its angular momentum.

Analysis of the available data shows that a self-consistent solution of the problem does not contain shock interaction between the matter stream from the libration point L_1 and the arising accretion disk ('hot spot'). Interaction of the disk halo gas and circumbinary envelope with the stream results in a shock wave at the edge of the stream. This shock wave (the so-called hot line) is readily apparent in Fig. 7a, b.

The tidal impact of the donor star gives rise to the spiral shock wave shown by the dotted line in Fig. 7a. The solution with a high gas temperature contains only one arm of the spiral shock wave; the flow structure in the region where another arm ought to be present is determined by the matter stream from L_1. It is worthy of note that in this case, the tidal spiral wave enters deep into the disk interior.

We consider matter flow morphology in a semidetached binary system with a stationary cold ($T \sim 1.4 \times 10^4$ K) disk. Figure 7c depicts the distribution of density and velocity vectors in the system equatorial plane. Shock waves arising in the disk are seen in Fig. 7c as confluent density isolines. The closeness of isolines at the disk edge corresponds to a sharp decrease in density, from characteristic disk values to background ones. Figure 7d, e depicts the enlarged region of the stream – halo interactions in the equatorial plane; density isolines and velocity vectors are shown in Fig. 7d and the field of velocities in Fig. 7e. It can be seen that the interaction between the circumdisk halo and the stream has all the typical characteristics of an oblique collision of two streams. The resulting structure of two shock waves and the tangential discontinuity separating them is well apparent in Fig. 7d, e. The region of shock interaction between the gas of the disk halo and the stream lies outside the disk and has an intricate shape. Parts of the halo distant from the disk have low density and their interaction with the stream runs generates a shock wave at the edge of the stream. The shock wave bends as the halo gas density increases and eventually finds itself located along the stream edge. The shock wave is sufficiently long and may be called a hot line. It follows from the above general characteristics of the stream flow pattern that in the interaction region, the halo gas and the stream gas pass through shock waves and intermingle; the resulting mixture travels along the tangential discontinuity between the two shock waves. Thereafter, this material is used to build up the disk proper, the halo, and the circumbinary envelope.

These peculiarities of the stream flow in systems with hot and cold accretion disks are schematically presented in Fig. 8a, b, showing part of the donor filling its Roche lobe, the position of the libration point L_1, the stream of matter outflowing from L_1, and the location of the accretor. A three-dimensional gasdynamic computation demonstrated that the solution for a cold accretion disk has the same qualitative features as the solution for high temperatures: the stream – disk interaction is shock-free, and the region of enhanced energy release (shock wave, HL) resulting from interactions between the disk halo gas and the stream is situated outside the disk. At the same time, the cold accretion disk (zones A and B in Fig. 8) is much denser than stream matter, its height diminishes, and the shape changes from quasielliptical to practically circular. The circumdisk halo (zone C in Fig. 8) also contracts significantly. The second arm of the tidal spiral shock wave forms, but neither arm reaches the accretor; both stay in the outer regions of the disk.

3.2 Precession density wave in cold disks

Bearing in mind that the stream of matter has only a weak influence on the dense inner parts of the disk and that shock waves (the hot line and two arms of the tidal waves) are located at the disk periphery, one more element of the flow structure can be distinguished in the cold solution: it is the inner region of the disk (zone A in Fig. 8) where the effect of the aforementioned gasdynamic perturbations may be neglected. We consider the behavior of matter in the inner disk regions unexposed to gasdynamic perturbations. In the absence of external impacts, a particle revolves around a gravitating center (accretor) in an elliptic orbit. It is known (see, e.g., Ref. [38]) that the effect of the second component in a binary star is the retrograde precession of the particle orbit as it revolves around the accretor (i.e., revolution of the major semiaxis of the orbit against the orbital motion); the precession rate decreases as the particle approaches the accretor.

An accretion disk is formed of many particles, each traveling in its own elliptical orbit. Because the particles interact with one another and form a gas, the disk should be considered in the gasdynamic approximation, necessitating transformation from orbits to flow lines, also elliptical in shape. As is known, there can be no mutually perpendicular intercrossing stream flows in a gas; therefore, flow lines can be only tangential to one another.

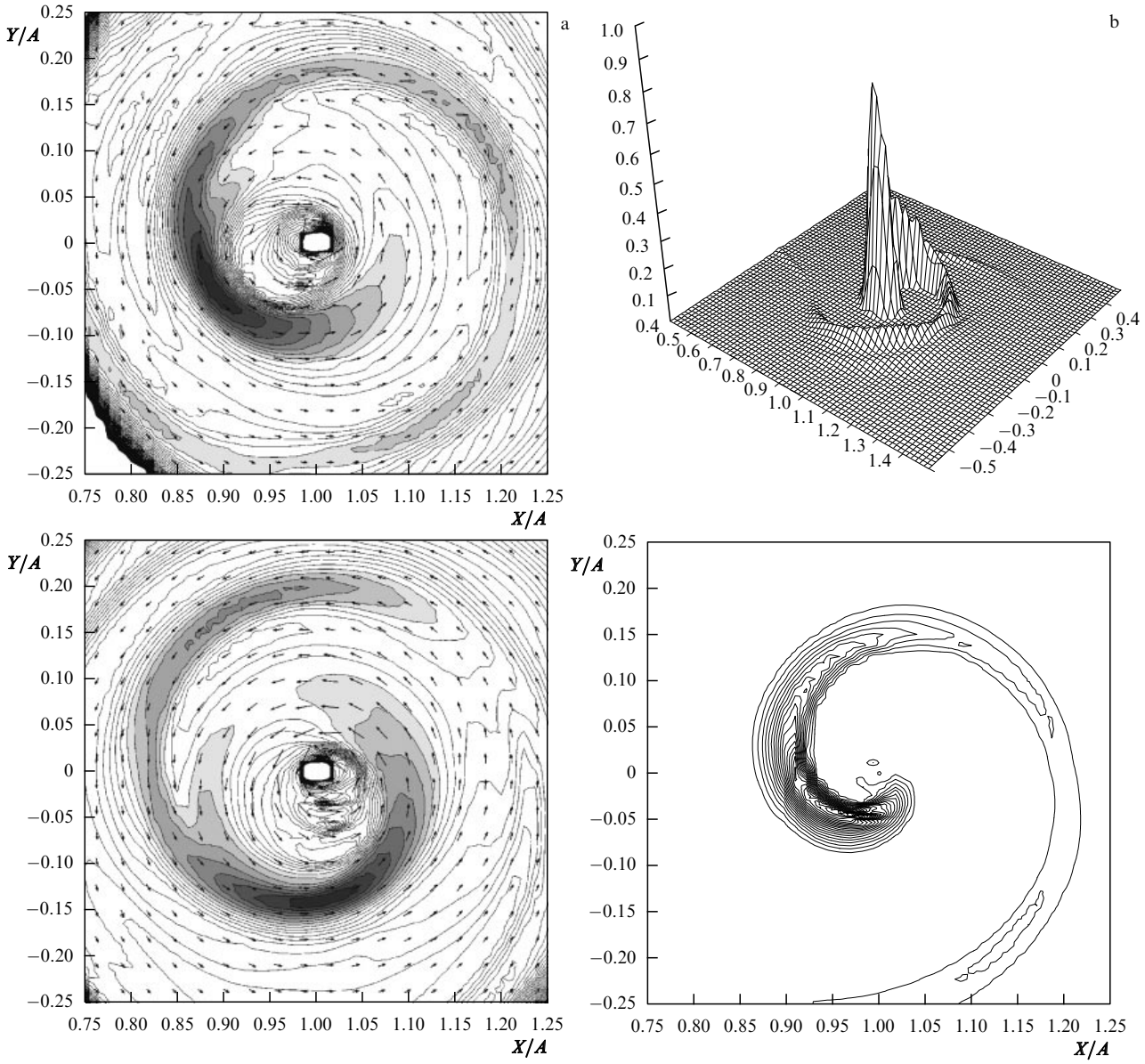

Figure 9. (a) Density isolines and velocity vectors in the equatorial plane of a system (in the region marked by the hatched square in Fig. 7c) for two instants of time differing by 1.5 orbital periods. (b) Distribution of a radial matter flow over the disk toward the accretor; the flow is normalized by its maximum value.

It is clear from geometric reasoning that a disk of disjoint ellipses can be constructed only by fitting one ellipse into another. A round disk is formed in this way given zero eccentricity of all elliptic flow lines. In the case of a nonzero eccentricity of these lines, an 'equilibrium solution' is feasible in which major semiaxes of all flow lines lie on the same straight line. If the system contains an external factor (inevitable in a binary star) and the orbit precession rate increases as the major semiaxis lengthens, flow lines distant from the accretor outrun those with smaller semiaxes. Because there can be no intercrossing stream flows in a gasdynamic disk, an equilibrium is reached after a time and all the lines start precessing with the same angular rate, i.e., in a solid-state mode. Because precession is retrograde and its rate depends on the characteristic size of the orbit, flow lines distant from the accretor must rotate through a larger angle and opposite to matter rotation.

The precession rate varies from that of outer ('fast') orbits to the precession rate of inner ('slow') orbits. The position of an inner orbit is determined by the fact that the effect of the second component in this disk region is negligibly small compared with that of the accretor gravitational field and may be disregarded. The position of the outer orbit is given by the size of the region free from gasdynamic perturbations because perturbations tend to disturb the regularity of flow line precession. Clearly, the position of both inner and outer orbits depends on the system parameters proper and on the parameters of mass exchange. Therefore, the mean rate of precession can be expected to differ in different systems. The formation of spiral structures in accretion disks is considered in Refs [68, 73, 74].

Analysis of the aforementioned results of three-dimensional numerical modeling (Fig. 7c) confirms the hypothesis of spiral density wave formation in the interior of a cold disk. Figure 9a describes the propagation of this wave, showing distribution of density and velocity vectors in the equatorial plane of the system for two time instants differing by 1.5 orbital periods. The two-arm spiral wave rests in the

noninertial reference frame connected with the binary star, whereas the precession wave slowly propagates in the laboratory system of coordinates (the stationary observer reference frame); its rotation period in the noninertial reference frame is slightly longer than the orbital period. Figure 9b shows two variants of the motion of a radial matter flow over the disk toward the accretor in the equatorial plane of the system. The flow is normalized by its maximum value. Evidently, the line connecting the peaks of the matter stream toward the accretor looks like a spiral. Due to an increase in the radial matter flow behind the precession density wave, the accretion rate increases roughly by one order of magnitude compared with its value in the solution disregarding such a wave.

Perfect agreement between the results of qualitative analysis and the theory definitively confirms that this wave is produced by the precession mechanism.

3.3 Density wave in hot disks

It was found in Refs [65, 75] that even a small alteration of the mass exchange rate in a binary system perturbs the equilibrium of the hot accretion disk and gives rise to a bunch of matter traveling over the disk at a velocity roughly 6 times $\Omega_{\rm orb}$ (Fig. 10).

The results of computations indicate that the bunch is a long-lived structure whose average characteristics remain unaltered at times of the order of tens of orbital periods of the system. This situation is illustrated by Fig. 11 showing time-dependent variations in the average density of matter passing through the halfplane perpendicular to the system plane that cuts the disk along the line connecting the components in the direction from the accretor to the outer Lagrange point (plane XZ, $Y = 0, X > A$). The three curves in Fig. 11 describe a 2-, 10-, and 10^5-fold decrease in the mass transfer rate (top, intermediate, and bottom curves, respectively). Evidently, the general alteration of density is accompanied by its quasiperiodic fluctuations caused by the traveling bunch. Analysis of the above curves indicates that a change (decrease) in the mass transfer rate is followed by the formation of a compact mass that moves in the disk with the period $\sim (0.15-0.18)P_{\rm orb}$. It can be concluded from the previously cited data that the bunch does not spread out under the action of dissipative processes ($\bar{\rho}$ changes only in the initial transition period), and its rotation frequency remains practically unaltered until the disk disappears.

Papers [33, 76] give evidence of the wave nature of this bunch, which is actually nothing but a single-arm spiral density wave. It is known from the well-developed theory of galactic spiral density waves that such a wave rotates in a solid-state mode and is not extended by differential rotation.

As mentioned in the Introduction, the flow of matter in a binary system is determined by the field of forces given by Roche potential (1). To clarify the bunch nature, we first consider oscillations that the gravity potential can excite in the disk plane. We subtract the spherically symmetric potential of the accretor $\Phi_{\rm A}$ from the total potential, $\tilde{\Phi} = \Phi - \Phi_{\rm A}$, and examine the Fourier spectra in the azimuthal harmonics of $\tilde{\Phi}$ in different radial regions of the disk. Figure 12a shows amplitudes of the Fourier spectrum components of $\tilde{\Phi}$ for different radial regions of the accretion disk. Evidently, the entire region under consideration is dominated by the harmonic $m = 2$. The predominance of the second harmonic reflects the character of the tidal influence of the donor, also confirmed by the monotonic

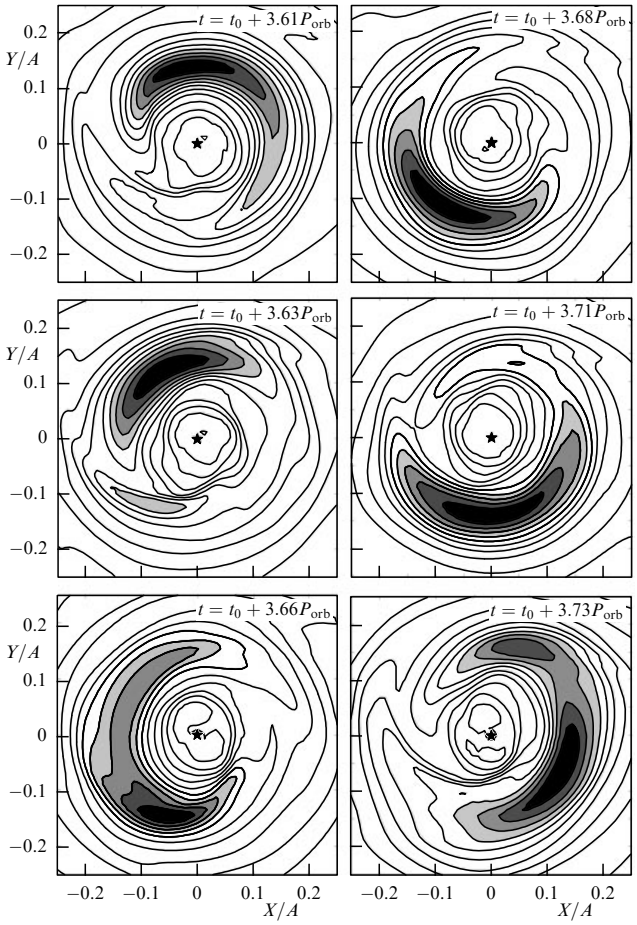

Figure 10. Density distribution in the equatorial plane of a system near the accretor (black star) for six instants of time (indicated in the figure) throughout the bunch orbital period. The density maximum for all distributions is $\rho_{\rm max} \simeq 0.035\rho(\mathrm{L}_1)$.

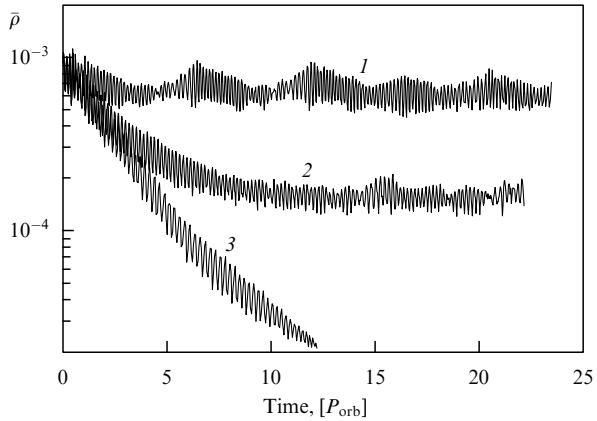

Figure 11. Curves showing time-dependent variations in the average density of matter passing through the halfplane perpendicular to the system plane that divides the disk along the line connecting the components from the accretor to the outer Lagrange point. Curve *1* corresponds to a 2-fold decrease in the mass transfer rate, curve *2* to a 10-fold decrease, and curve *3* to a 10^5-fold decrease.

increase in the absolute value of the potential with increasing the disk radius. The maximum absolute value of the nonspherical part of the potential is recorded in the peripheral disk region closest to the donor.

However, results of calculations show convincingly that the gravity force is not crucial for the distribution of disk

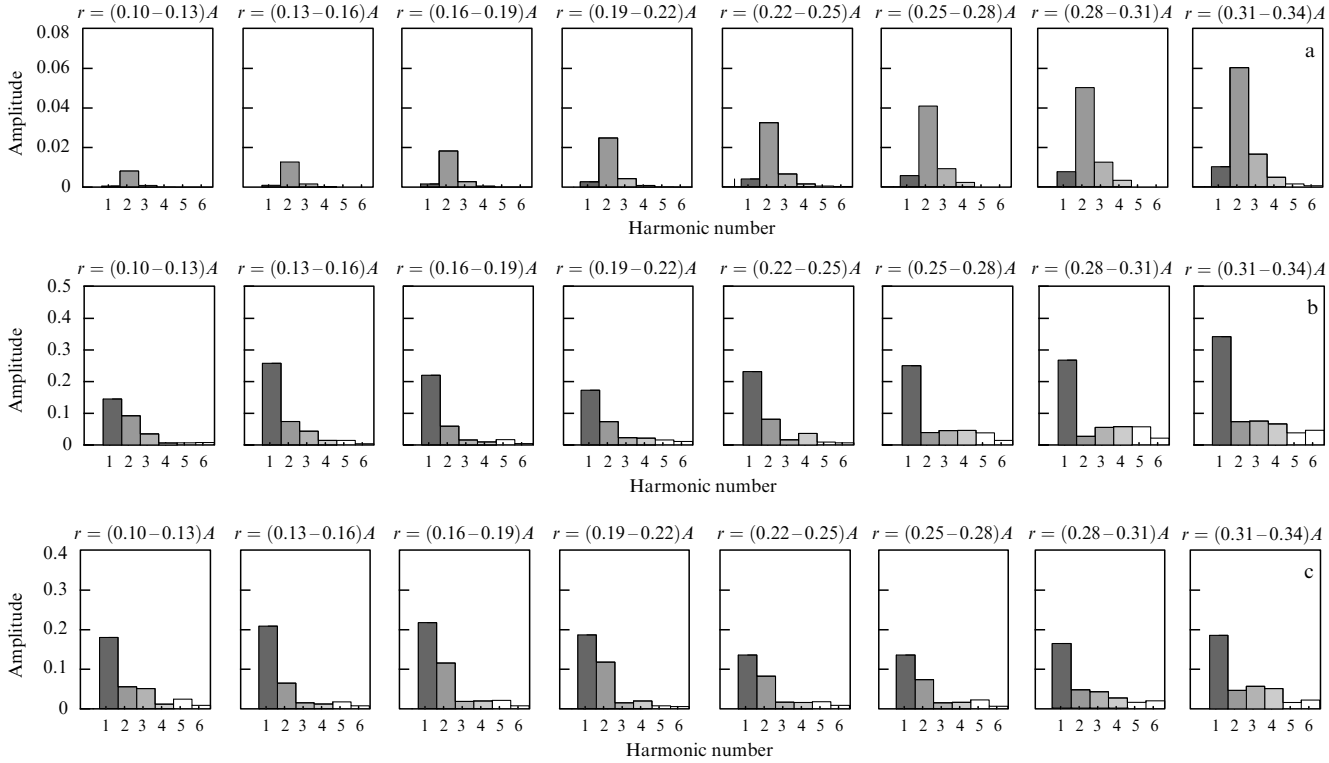

Figure 12. (a) Relative amplitudes of the first five Fourier spectrum components of the nonaxisymmetric part of the potential for different radial equatorial regions of the accretion disk. (b) Relative amplitudes of harmonics of the nonaxisymmetric part of the 'refined' surface density for different radial equatorial regions of the accretion disk. (c) Relative amplitudes of harmonics of the nonaxisymmetric part of the 'refined' radial velocity for different radial equatorial regions of the accretion disk.

matter. We consider the spectrum of the 'refined'[6] surface density $\tilde{\sigma}$ following the perturbation, i.e., after the mass exchange rate is altered and a bunch is formed in the accretion disk. The corresponding harmonics of the surface density spectrum are presented in Fig. 12b. Here, the Fourier spectrum of the surface density is dominated by the mode $m = 1$, in agreement with the presence of a compact mass. A similar picture is observed in the distribution of radial velocity harmonics (Fig. 12c).

Analysis of the maximum density phase curve of the first azimuthal harmonic of the density profile at different time instants shows that the position of the maximum-density phase curve of the $m = 1$ mode is at any time closely associated with the bunch. Moreover, consideration of all maximum-density phase curves of the first azimuthal harmonic of the density profile during the bunch orbital period (Fig. 13a) reveals that a curve does not appreciably change its shape after complete revolution. This observation suggests that differential rotation of the disk does not degrade this harmonic.

Taken together, the phase rotation velocity of the $m = 1$ mode differing from that of the tidal mode and the solid-state character of its rotation give evidence that the bunch is a spiral density wave. According to the theory of spiral density waves in galactic disks, a single-arm spiral wave is associated with an anticyclonic eddy having its center on the corotation radius (see, e.g., Ref. [77]). The center of the anticyclone must be located in the vicinity of the surface density maximum. Analysis of the field of velocities on the disk plane in a coordinate system connected with the bunch shows the presence of an anticyclonic eddy behind the compact mass (Fig. 13b). The center of the anticyclone marked by a black star is situated in the neighborhood of the surface density maximum (i.e., close to the bunch), in perfect agreement with the theory. Moreover, the center of the anticyclone lies exactly on the corotation circle (shown by the light solid line in Fig. 13b) as predicted by the theory of spiral density waves.

To summarize, the following argument leads to the conclusion that the $m = 1$ mode is a spiral-whirling single-arm structure.

(1) The $m = 1$ mode rotates with a phase velocity different from that of the tidal $m = 2$ mode.

(2) The $m = 1$ mode undergoes practically no deformation of the maximum disk surface density phase by differential rotation.

(3) Because the computed corotation radius of the $m = 1$ mode lies in the region strongly dominated by this mode, we could expect (in analogy with galactic disks) a single anticyclone with its center on the corotation circle and in the respective region (i.e., in the vicinity of surface density maximum). The anticyclone actually turned out to be located exactly in this region of the disk.

3.4 Observational manifestations of waves in accretion disks

3.4.1 Hot line. Analysis of light curves is one of the most informative methods for the study of CBSs. The short orbital period (a few hours) of these stars allows determining the major properties and characteristic parameters of the processes proceeding in the system in a relatively short observational time. Light curves of an eclipsing CBS have

[6] The 'refined' function is found by subtraction of the period-averaged distribution.

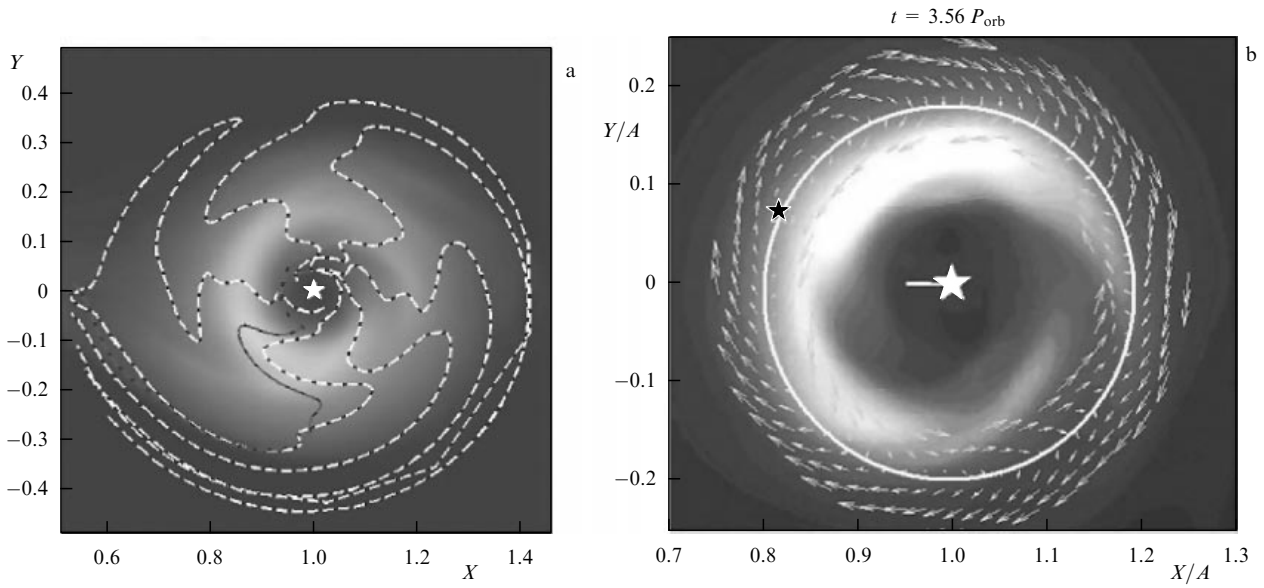

Figure 13. (a) Phase curves of maximum density of the first azimuthal harmonic in the density profile during the bunch orbital period in the orbital plane; dark solid line is the phase curve of maximum density by the moment the bunch completes revolution. The star marks the accretor. (b) The density and velocity distribution in the equatorial plane in the system of coordinates connected with the bunch at the time instant $t = 3.56P_{\rm orb}$. Light and dark stars respectively denote the accretor and the center of the anticyclone. The segment originating in the accretor is directed toward the donor star. The light solid line shows the corotation circle on which the phase velocity of the single-arm spiral wave coincides with the disk rotation velocity.

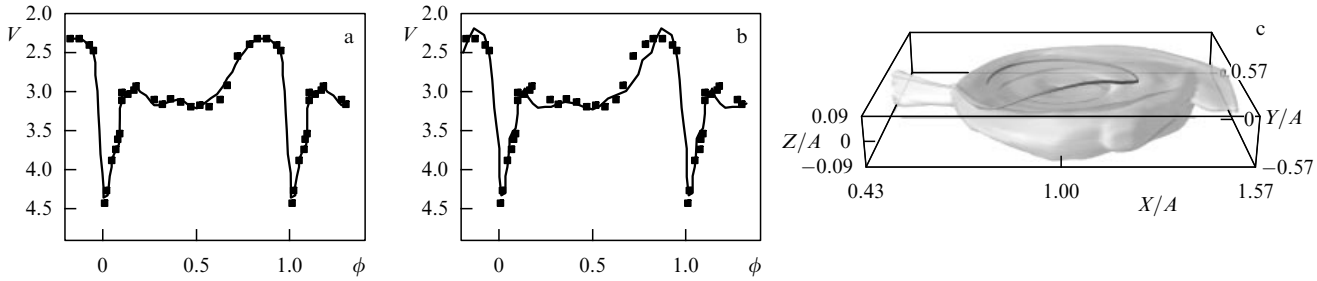

Figure 14. (a, b) Average light curve (squares) of IP Peg at rest, in the V-filter. Synthetic light curves calculated in the hot-line (a) and hot-spot (b) models are shown as solid lines. (c) Three-dimensional density isosurface at $\rho = 5 \times 10^{-11}$ g cm^{-3}; also shown is a section of the flow line originating in the vicinity of L_1.

additional peculiar features that cannot be explained in terms of the 'cold star – white dwarf – accretion disk' model. Specifically, most light curves of eclipsing CBSs show the so-called hump. It was suggested in [78, 79] that the hump is produced by the glow of the hot spot arising at the border of the accretion disk where a stream of matter from L_1 hits it. During the last 30 – 35 years, the hot-spot model has been widely used to interpret light curves of cataclysmic binary systems.

Gasdynamic studies of matter exchange in CBSs have shown (see Section 3.1) that the stream and the accretion disk make up a morphologically integrated entity and interact in a shockless manner. Naturally, there is no temperature increase in the stream – disk contact region, and the hot-spot hypothesis is inapplicable to the explanation of humps on the light curves of eclipsing CBSs. Three-dimensional computation of the structure of matter flow in an interacting CBS indicates that shock interaction in the stationary case causing an increase in temperature occurs when the stream of matter outflowing from L_1 collides with the circumdisk halo. This interaction produces an extended shock wave (hot line) whose emission may be used to explain effects observed on the light curves of cataclysmic variables, such as the appearance of normal and abnormal humps when the donor star eclipses the accretion disk

The solution of the inverse problem of interpreting eclipsing light curves of cataclysmic variables in the framework of two alternative models demonstrates that the hot-line model describes the observed light curves better than its hot-spot counterpart, both in a quiescent system and in a superflare (see, e.g., Refs [80 – 83]).

The two models are compared in Fig. 14a, b showing the observed and synthetic light curves for the system IP Peg at rest, in the V-filter. The hot-line model better reproduces the hump width on the light curves, the eclipse type, and the details of noneclipsing brightness changes. Comparison of the hot-spot and hot-line models convincingly confirms the advantages of the latter for the interpretation of CBS light curves. This means that a theoretical shock wave (hot line) is in fact a real structure of accretion disks in CBSs.

Other evidence of the existence of the hot line was obtained in a study of dips in the light curves of semidetached binary systems with stationary disks [71].

Observations of low-mass X-ray binaries (LMXBs) have revealed dips in the X-ray light curves of certain systems. There have been attempts to explain these dips in terms of a

hypothesis that postulates a thickening at the outer edge of accretion disks with the phase ~ 0.8 corresponding to the position of this feature on the light curve. The presence of matter surrounding the X-ray source very high above the orbital plane of the system coupled to its nonuniform distribution along the azimuth may be attributed either to the gravitational action of the companion on the accretion disk or to the interaction of the matter stream from L_1 with the disk. The coincidence of the phase of the observed dips with the postulated location of the region in which the stream from L_1 approaches the outer edge of the disk has attracted the attention of researchers to this region. Today, the appearance of matter at heights much larger than the disk thickness is most plausibly explained by a rebound of the stream from the outer edge of the disk. This explanation also holds for the presence of dips on the light curves of LMXBs.

Dips in the light curves produced by the appearance of matter in certain places high above the disk are most readily identified in LMXBs because LMXBs have a very compact source in the disk center. At the same time, similar features of light curves in different wavelength ranges were recorded in many other cataclysmic binary systems during a flare (U Gem, OY Car, Z Cha). Further studies have shown that dips in the light curves may just as well occur in steady-state systems. This hypothesis was confirmed by observations of UV light curves of eclipsing cataclysmic binary systems UX Uma and RW Tri [84]. These findings suggest the universal character of this phenomenon in semidetached binary systems with accretion disks. Interestingly, stars with stationary disks, unlike explosive systems, exhibit preeclipsing dips in much earlier phases, $0.6-0.7$ [84, 85].[7]

The question is: what causes the presence of matter much above the accretion disk in the case of its steady-state interaction with the stream? Results of gasdynamic studies of the established stream flow in semidetached binary systems suggest the shockless nature of such interaction. In this situation, unlike in the nonstationary case (hot-spot model) where the stream is supposed to hit the disk edge, the stream interacts with the gas of the disk halo and forms an extensive region of enhanced energy release (hot line). This means that no rebound of the stream occurs in the established regime, and this effect cannot be used to account for the dips in the light curves of binary systems with stationary disks.

Examination of disk halo thickness in CBSs with stationary disks in Ref. [71] demonstrated thickening of the halo above the disk even in the absence of its direct collision with the stream. In the gasdynamic flow pattern described by the hot-line model, a large fraction of matter undergoes vertical acceleration in the course of the stream–halo interaction. Vertical motion of the gas induced by the z-component of velocity coupled to its motion along the outer edge of the disk causes a gradual increase in the halo thickness. The vertical acceleration region is delimited by the hot-line region, whose angular dimension does not exceed $\sim 65^\circ$. But the gas that passed this region acquires a large vertical component of velocity that causes it to ascend progressively until its kinetic energy is exhausted. The point at which the vertical motion stops lies at a maximum height and corresponds to the phase ~ 0.7, i.e., it is located far beyond the hot line. The height of the thickening is several times the characteristic height of the disk and can reach $\sim 0.04A$ (this value corresponds to the ratio of the height of the thickening to its distance from the accretor > 0.1); its angular dimension exceeds $\sim 130^\circ$. The estimated maximum of the halo thickness over the outer edge of the disk falls within the phase ~ 0.7 (Fig. 14c), in agreement with the observed values for cataclysmic variables with stationary disks. This finding confirms the validity of the hot-line model proposed earlier for the description of matter flow in semidetached binary stars and opens up the possibility for interpreting the light curves of such systems.

3.4.2 Spiral tidal wave. The use of gasdynamic models combined with Doppler tomography allows identifying the main flow elements on Doppler maps without solving an ill-posed problem.

In recent years, results of observations of binary systems have been extensively used in the form of serial spectrograms of a selected emission line, $I(\lambda, t)$ [in other words, $I(V_R, \phi)$]. Doppler tomography is the best method for the analysis of such spectrograms [86], allowing orbital variability of the emission line intensity to be converted to a luminosity map in the two-dimensional velocity space. The Doppler tomogram is a product of the transformation of a series of spectrograms obtained at successive time instants $I(V_R, t)$ [or at sequential orbital phases $I(V_R, \phi)$, which is the same]. A Doppler map is easier to interpret than initial spectrograms; in certain cases, it reveals details of the flow structure, or at least offers suggestions. For example, lines with a two-hump profile corresponding to circular motion (e.g., in the accretion disk) turn into a blurred circle on the Doppler map. In other words, components of a binary system are resolved in the velocity space, although they cannot be spatially resolved by direct observations. Thus, Doppler tomography provides a powerful tool for the study of binary systems.

Unfortunately, the problem of reconstructing the spatial distribution of the emission line intensity with the use of Doppler maps has no solution in the general case because points spaced far apart may have equal velocities and contribute to the same region of the Doppler map. For this reason, the transformation $I(V_x, V_y) \to I(x, y)$ is impractical without certain a priori assumptions regarding the structure of the velocity field.

The situation changes dramatically when Doppler tomography is supplemented by gasdynamic calculations [87]. In this case, there is no need to solve the inverse problem because the Doppler tomogram can be obtained directly: $\rho(x, y) - T(x, y) \to I(x, y)$ and $I(x, y) - V_x(x, y) - V_y(x, y) \to I(V_x, V_y) \to I(V_R, \phi)$.

Recently, a large number of publications were devoted to the binary system IP Peg and the analysis of its Doppler tomograms. One generally recognized conclusion from these observations is the absence of the traditional hot spot in IP Peg, in agreement with the hot-line model considered in this review. Observational Doppler tomograms of IP Peg are categorized into two groups: for the system in a quiescent state and for that in an active state. The dwarf nova IP Peg produces flares with a period of approximately 3 months, the flare duration being about 10 days and the resting state around 80 days (~ 60 and ~ 480 orbital periods, respectively).

Tomograms obtained for the system at rest correspond to solutions with a hot accretion disk. The intensity distribution in the equatorial plane of IP Peg at rest and synthetic Doppler maps are presented in Fig. 15a, b.

[7] The phase angle ϕ is referenced as in the analysis of observational data, to the line connecting the centers of the stars in the direction opposite to the rotation of the system.

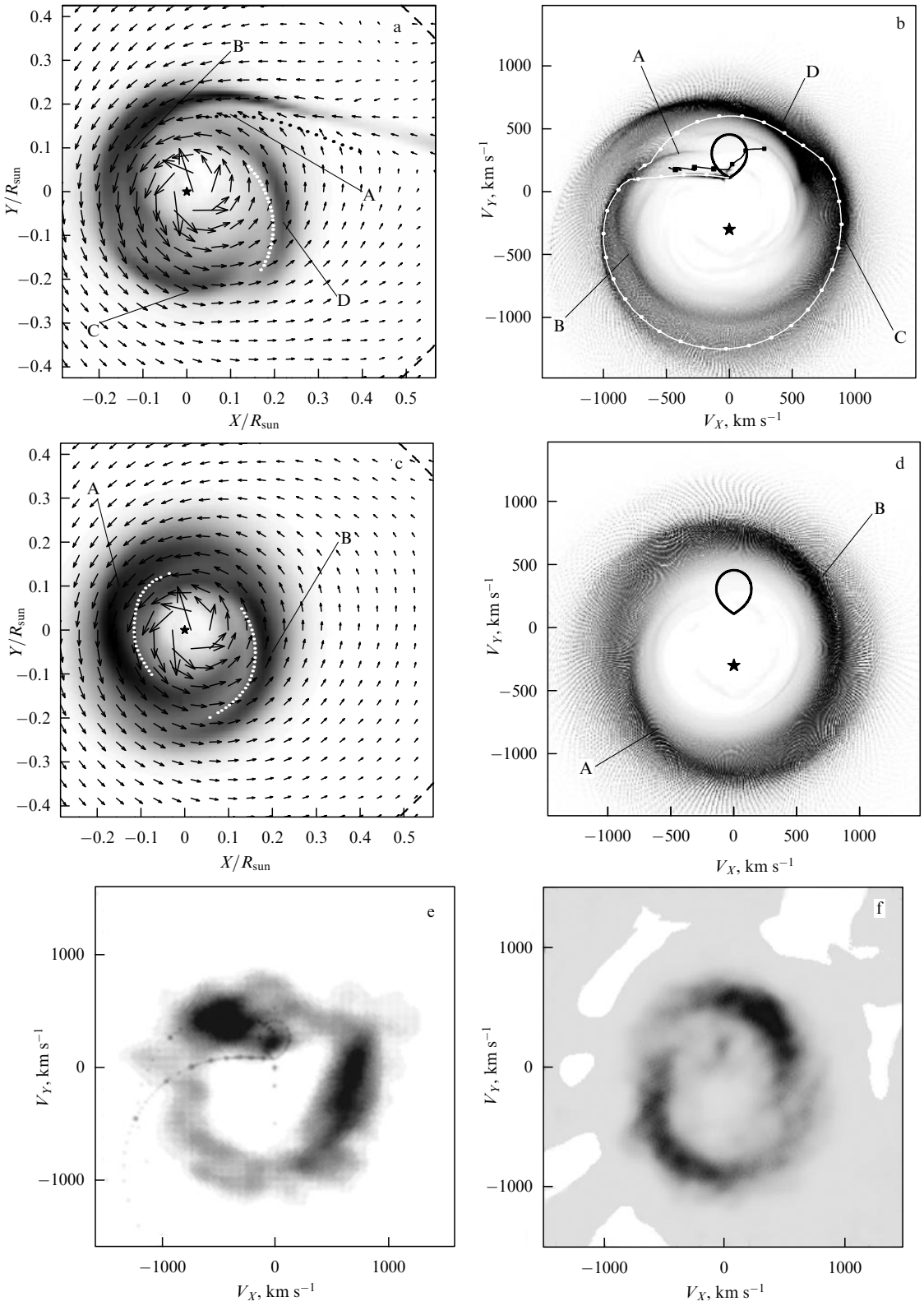

Figure 15. (a) Intensity distribution in the equatorial plane of IP Peg at rest; A, B, C, and D, zones of maximum radiation intensity; A, hot line; B, stream; C, the apogee of the quasielliptical accretion disk; D, an arm of the spiral tidal wave. (b) Synthetic Doppler map for IP Peg at rest: the Roche lobe of the donor star and accretor are respectively shown by the thick solid curve and the star. A, B, C, and D are the same zones as in (a). (c) Intensity distribution in the equatorial plane of IP Peg in the active state; A and B are zones of maximum radiation intensity, the two arms of the spiral tidal wave. (d) Synthetic Doppler map for IP Peg in the active state: the Roche lobe of the donor star and accretor are respectively shown by the thick solid curve and the star; A and B, C are the same zones as in (c). (e, f) Doppler tomograms of IP Peg in quiescent (e) and active (f) states [88, 89].

Summarized results of the analysis of a synthetic Doppler tomogram of the quiescent IP Peg lead to the conclusion that the main contribution to luminosity is made by four elements of the flow: the hot line, the brightest part of the stream

from L_1, the compact mass near the apogee of the disk, and the compact mass behind the arm of the spiral shock wave. Evidently, the contribution of these elements to the total luminosity differs depending on specific features of the system of interest. It is equally understandable that based on the results of model calculations, it is impossible to say which element prevails in the system. Nevertheless, comparison of synthetic and observed tomograms may help to answer this question, determine the parameters of the gasdynamic model that need correction, and clarify details of the flow pattern in the system.

A typical example of an observational Doppler tomogram for the quiescent state of the system is presented in Fig. 15e [88]. Characteristic features of such tomograms are a bright spot in region A and enhanced brightness of region C (Fig. 15a). Comparison with a synthetic tomogram (Fig. 15b) shows that the main contribution to luminosity on the observational tomogram of IP Peg at rest is made by the shock wave at the edge of the stream (i.e., the hot line) and the compact mass near the apogee of the disk. Contributions from the spiral wave and matter stream are small.

The flow structure in the active state can be assessed from the solution with a cold accretion disk. The intensity distribution in the equatorial plane of IP Peg in the active condition and the synthetic Doppler map are presented in Fig. 15c, d. In this case, two arms of the spiral tidal wave are the main contributors to luminosity. A typical example of an observed Doppler tomogram for the active state of the system is presented in Fig. 15f [89]. Characteristic features of such tomograms are bright spiral arms in two quadrants of the Doppler map. It follows from the comparison with Fig. 15c, d that in the active state, both bright spots are due to the emission of radiation from high-density regions located behind the two arms of the spiral tidal shock wave.

Comparison of the observed and synthetic tomograms permits not only verifying the gasdynamic model but also identifying shock waves in accretion disks of CBSs. The tomograms show both the hot line and the arms of the spiral tidal wave.

3.4.3 Precession spiral density wave in cold disks. It is known from gasdynamic calculations that the formation of a precession density wave in a disk is followed by a very sharp increase in the accretion rate (up to several orders of magnitude), leading to a flare. Matter comes up to the surface of the accretor along the precession wave; therefore, the region where it accretes is localized in azimuth and looks like a luminous spot on the accretor surface. The light curve acquires a hump. The wave slowly precesses in the stationary observer reference frame and causes a shift of the region with the enhanced accretion (i.e., the hump) upon each new revolution of the system. The period of the hump is determined by beats between the orbital period of the system and the precession period of the wave.

These phenomena are actually observed in certain systems. Superhumps, i.e., modulations on the light curve of a binary system, whose period differs by several percent from the orbital period, largely occur during superflares in systems of the SU UMa type. The main observational features of superhumps are described in monograph [38]. A number of models have been proposed to explain the phenomenon of superhumps (their brief characteristics and criticism can be found in Ref. [38]). The currently most popular model attributes these variations in brightness to the precession of the outer parts of the accretion disk. The Lindblad 3 : 1 resonance present in the disk causes an instability that gives rise to precession of its outer regions with the period several times the orbital period. Beats between the two periods, orbital and precessional, are responsible for periodic oscillations of brightness manifested as a superhump. We note that this model is not free from drawbacks, the most important being the limitation on the maximum value of the component mass ratio. For the Lindblad 3 : 1 resonance to be present inside the accretion disk, this ratio q (the donor-mass to accretor-mass ratio) must not exceed ~ 0.33 [90]. But there are systems in which superhumps are observed at a significantly higher q. They are exemplified by TV Col with q in the range $\sim 0.6-0.9$.

In 2004, a new mechanism of superhump formation was proposed for SU Uma-type systems, assuming the generation of a precession density wave in the accretion disk [69]. The superflare model postulates the presence of a precession spiral wave in the accretion disk. It permitted the first explanation of all meaningful observational manifestations of superflares and superhumps in the systems of the SU Uma type, including the period, length, energy release, anticorrelation of brightness and color temperature at an ordinary superhump maximum, and the 'late superhump' phenomenon. Moreover, the new model places no strict limitation on the component mass ratio in a binary system and can be used to explain the superhump formation mechanism in systems with a large mass ratio, up to $q = 0.93$.

3.4.4 Spiral density wave in hot disks. A bunch rotating in the accretion disk manifests itself as a change in the brightness of the CBS. Eclipsing cataclysmic variables with large orbital plane angles are good candidates for the search for a bunch. It can be supposed that the presence of a bunch rotating in the accretion disk is a cause of brightness fluctuations in noneclipsing sections of light curves. We chose to search for observational evidence of a single-arm spiral density wave in the accretion disks of systems IP Peg and WX Ari. IP Peg is an eclipsing cataclysmic variable with the orbital period 3.8 h. The component mass ratio of the system is $q = 1.7$, and the orbital plane angle is $\sim 68^\circ$. The system WX Ari II is likewise an eclipsing cataclysmic variable with the orbital period 3.34 h and the orbital plane angle $\sim 72^\circ$. Fluctuations in brightness in noneclipsing regions of the light curves are apparent even at a superficial glance, but Fourier analysis is needed for precise measurements.

Figure 16 presents light curves of IP Peg [88] obtained 5 and 6 days after a flare in the continuum, lines H_β, H_γ, HeI 4472 Å, and HeII 4686 Å. Fourier analysis shows that the maximally distinguished harmonic in the curves has the frequency $5.5\,\Omega_{\rm orb}$. These spectral characteristics of light curves reflect the presence of a spiral density wave in the accretion disk of the cataclysmic variable IP Peg; the wave rotates with the frequency 5.5 times the orbital frequency of the system. The light curve in line HeII most obviously demonstrates the presence of a bunch because the density wave of high optical density propagating over the accretion disk periodically blots out the view of the hot region emitted in this line between the wave and the second component. The same phenomenon is less noticeable in the light curve for the continuum.

In-depth studies of light curves in cataclysmic variables revealed similar harmonics in other objects of this class, e.g., WX Ari. Light curves of WX Ari are dominated by the

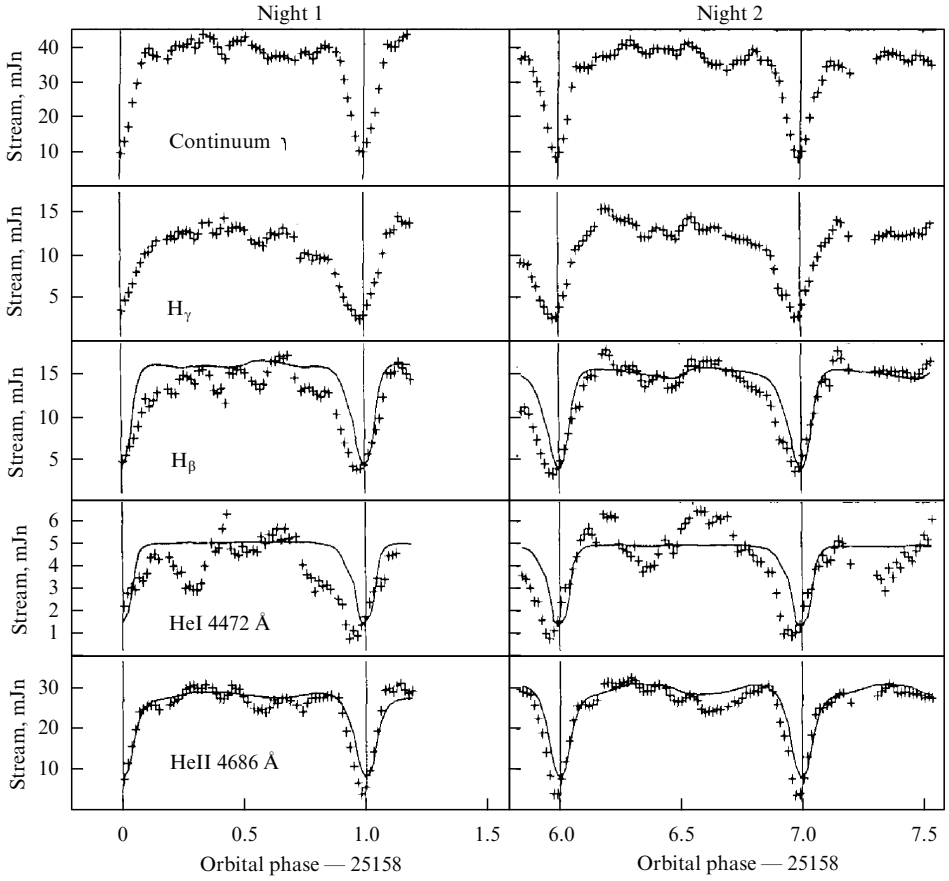

Figure 16. Light curves of IP Peg [88] in the continuum, lines H_β, H_γ, HeI 4472, and HeII 4686 Å.

harmonic with the frequency around $6.25\,\Omega_{\rm orb}$. Thus, analysis of light curves actually observed in cataclysmic variables with characteristics matching those of a numerical model reveals variations in brightness in the noneclipsing part of these curves with the frequency about 1/5 of the orbital period, in agreement with the theoretical orbital period of the bunch.

4. Developed turbulence in accretion disks of close binary systems

4.1 Overreflection instability

Sections 3.3 and 3.4.4 show that periodic variations in the quasi-stationary regime of the accretion disk in three-dimensional numerical simulations are caused by a single-arm spiral vortex structure with the period $\tilde{T}_1 \simeq (1/6)P_{\rm orb}$ (in a coordinate system rotating with the angular velocity of the system). This period is not related to the period of the donor tidal interaction force. In this section, we show that the above-mentioned single-arm spiral vortex structure is generated by an overreflection instability in the accretion disk.

To clarify why this mode originates and to reduce the influence of tidal force, we undertook the following steps.

(1) The results of three-dimensional numerical simulations were transformed to a new coordinate system $\{x', y', z\}$ with the origin at the accretor. This reference frame rotates around the center of mass of the binary star following the motion of the accretor, with its axes remaining parallel to the axes of the inertial reference frame.[8] Next, the transformation to the $\{r, \phi, z\}$ frame was made (the plane $z = 0$ is shared by the new and the old reference frames).

(2) All distributions are integrated over z and averaged over the period $P_{\rm orb}$. In this way, we analyze the dynamics of small (linear) perturbations in an isolated two-dimensional model of a disk with stationary axisymmetric parameters $\sigma_0(r)$, $\Omega_0(r)$, $P_0(r)$, and $\Phi_0(r)$, which are the surface density, angular velocity, pressure, and gravity potential, respectively, in the plane $z = 0$ (see, e.g., Fig. 17a) [33, 76]. This two-dimensional model of the accretion disk inherits basic large-scale features of the initial three-dimensional disk but does not include the tidal effect caused by the gravitational influence of the donor.

An analysis of the parameters of the disk model shows that the radial distribution of specific (per unit mass) angular momentum has an important feature, a (smoothed) slope discontinuity around the radius where the region of a single-arm structure begins in the initial three-dimensional disk (see Fig. 17b). To understand the importance of the slope discontinuity in the radial distribution of the specific angular momentum,[9] we write the dynamic equations describing a perturbed state of the two-dimensional model of an isolated accretion disk in the new

[8] We note that the period of variations is $T_1 \simeq (1/5)P_{\rm orb}$ in the new reference frame.

[9] Obviously, the slope jump in the plot of specific angular momentum implies a slope jump in the plot of the angular velocity $\Omega_0(r)$.

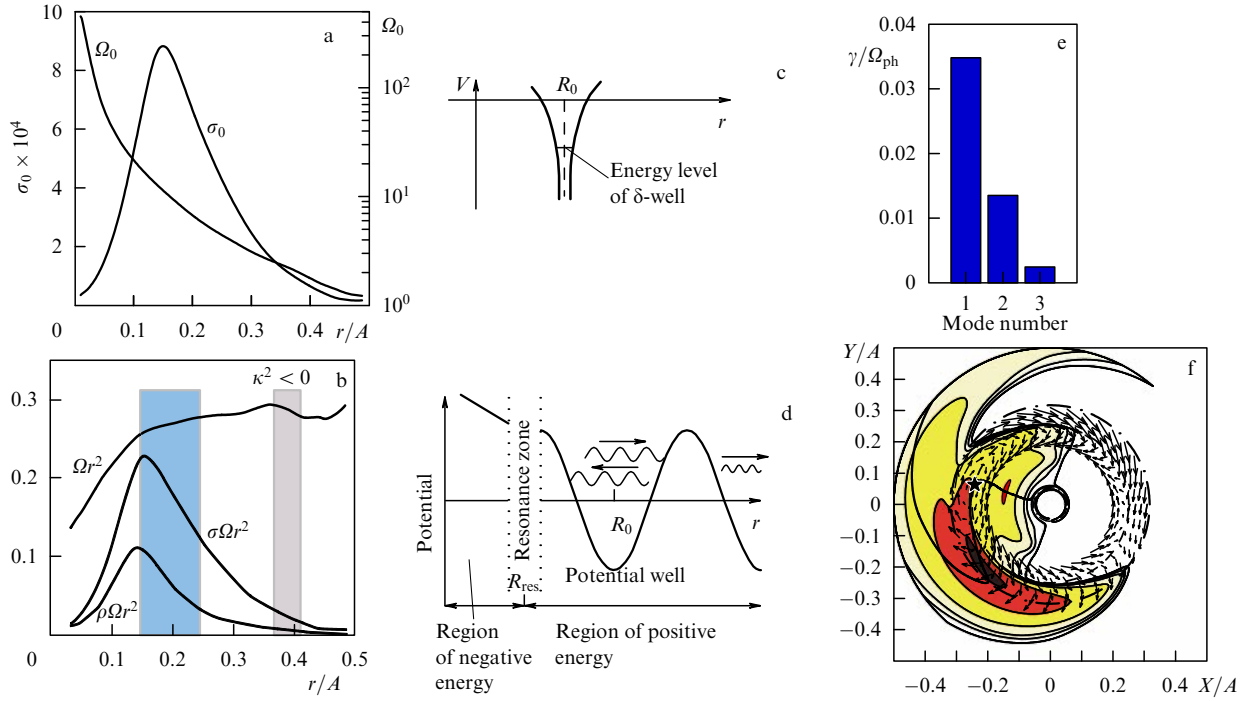

Figure 17. (a) The radial distribution of the surface density σ_0 (normalized to the density at the inner Lagrange point) and the angular velocity Ω_0 of the isolated model of a two-dimensional accretion disk in the new coordinate system. (b) Distributions of specific angular moment per unit mass (upper curve), unit surface (middle curve), and unit volume (lower curve); the left shaded rectangle shows the localization of the first (maximum-amplitude) harmonic. It is seen that the position of the slope jump in angular momentum curves is at the boundary of the region where the first harmonic is localized. (c) The energy level in a 'δ-well.' (d) An ordinary well where the incident and reflected waves are present. (e, f) The results of numerical analysis of linear modes generated by the overreflection instability in a two-dimensional model of an isolated accretion disk: (e) Increments of the first three large-scale modes ($m = 1, 2, 3$); (f) Eigenfunctions of the perturbed surface density [whose magnitude exceeds the background density $\sigma_0(r)$] and velocity perturbations (shown by arrows) for the most unstable single-arm spiral mode ($m = 1$)].

coordinate system:

$$\frac{\partial\sigma}{\partial t}+\frac{1}{r}\frac{\partial(r\sigma V_{\rm r})}{\partial r}+\frac{1}{r}\frac{\partial(\sigma V_\varphi)}{\partial\varphi}=0\,, \tag{27a}$$

$$\frac{\partial V_{\rm r}}{\partial t}+V_{\rm r}\frac{\partial V_{\rm r}}{\partial r}+\frac{V_\varphi}{r}\frac{\partial V_{\rm r}}{\partial\varphi}-\frac{V_\varphi^2}{r}=-\frac{1}{\sigma}\frac{\partial P}{\partial r}-\frac{{\rm d}\Phi_0}{{\rm d}r}\,, \tag{27b}$$

$$\frac{\partial V_\varphi}{\partial t}+V_{\rm r}\frac{\partial V_\varphi}{\partial r}+\frac{V_\varphi}{r}\frac{\partial V_\varphi}{\partial\varphi}+\frac{V_{\rm r}V_\varphi}{r}=-\frac{1}{\sigma r}\frac{\partial P}{\partial\varphi}\,, \tag{27c}$$

where σ is the surface density. Assuming that all the perturbed quantities are characterized by small deviations $\delta\tilde{F}$ from their unperturbed stationary values F_0,

$$F(r,\varphi,t)=F_0(r)+\delta\tilde{F}(r,\varphi,t)\,,$$

where

$$\delta\tilde{F}(r,\varphi,t)=\delta F(r)\exp\left[{\rm i}(m\varphi-\omega t)\right],$$

we can reduce the system of equations (27), after linearization, to an ordinary second-order differential equation for the enthalpy perturbation δW [91]:

$$\frac{\chi}{r\sigma_0}\frac{\rm d}{{\rm d}r}\left[\frac{r\sigma_0}{\chi}\frac{\rm d}{{\rm d}r}(\delta W)\right]-\frac{\chi}{r\sigma_0\hat{\omega}}\left[\frac{\rm d}{{\rm d}r}\left(\frac{2m\Omega_0\sigma_0}{\chi}\right)\right]\delta W$$
$$-\left[\frac{m^2}{r^2}+\frac{\chi}{c_0^2}\right]\delta W=0\,. \tag{28}$$

Here, the following notation is introduced:

$$\chi(r,\omega)\equiv\left[\hat{\omega}^2(r)-\varkappa_0^2(r)\right],\qquad \varkappa_0^2\equiv 2\Omega_0\left(2\Omega_0+r\frac{{\rm d}\Omega_0}{{\rm d}r}\right),$$

$$\hat{\omega}(r,\omega)\equiv\omega-m\Omega_0(r)\,,\qquad c_0^2\equiv\frac{\partial P_0}{\partial\sigma_0}\,.$$

In the limit case of a sharp slope discontinuity of $\Omega_0(r)$ at the radius $r = R_0$, its first derivative ${\rm d}\Omega_0(r)/{\rm d}r$ is proportional to $\theta(r - R_0)$, whereas its second derivative ${\rm d}^2\Omega_0(r)/{\rm d}r^2$ is proportional to $\delta(r - R_0)$, and hence

$$\frac{{\rm d}\chi}{{\rm d}r}\propto\frac{{\rm d}\varkappa_0^2}{{\rm d}r}\propto\frac{{\rm d}^2\Omega_0}{{\rm d}r^2}\propto\delta(r-R_0)\,.$$

Eliminating the first derivative from Eqn (28), we reduce it to the Schrödinger equation with a 'δ-well' [91], which always contains an energy level (Fig. 17c). In a real accretion disk, the δ-well transforms into an ordinary well (Fig. 17d). In this case, the potential well hosts two waves, the incident and reflected ones. The latter is reflected from the resonance layer (the vicinity of the corotation circle) with an increase in its amplitude. The additional kinetic energy is drawn from the kinetic energy of disk rotation, which increases in approaching the center. This leads to the overreflection instability that generates a single-arm density wave [91].

To explore the spiral density waves excited in the accretion disk by the overreflection instability, the boundary-value problem for Eqn (28) was solved numerically. In particular, the eigenvalues of this problem were computed giving the

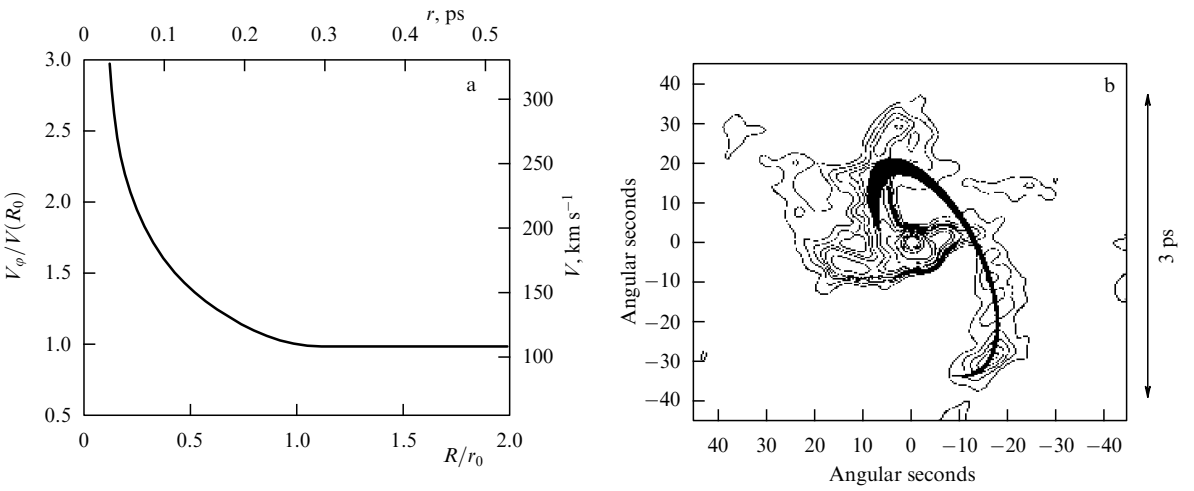

Figure 18. (a) The observed rotation velocity of the 'nuclear' disk in the center of our Galaxy. (b) Isophots (thin lines) of the disk in the center of our Galaxy. Their closeness correlates with the position of the 'mini-spiral.' The thick line superimposed on the pattern of isophots shows the single-arm spiral density wave obtained in Ref. [92] and caused by the overreflection instability.

angular phase velocity $\Omega_{\rm ph} \equiv {\rm Re}\,(\omega)/m$ and the instability increment $\gamma \equiv {\rm Im}\,(\omega)$.

A comparison of the main results obtained in the framework of the two-dimensional disk model with the respective results of numerical simulations of the accretion disk in a binary system shows that they practically coincide [33, 76]. The results obtained in the linear approximation are illustrated in Figs 17e, f. Figure 17e displays instability increments of the first, second, and third modes in units of the phase velocity $\Omega_{\rm ph}$. Figure 17f shows the main eigenfunctions for the most unstable single-arm spiral ($m = 1$). The perturbed surface density (only the excess over the stationary background) is represented by shading, and the solid curve is the phase curve of the maximum surface density. The perturbed velocity vector field (in the reference frame corotating with the single-arm mode) is displayed with arrows, and the star marks the center of the anticyclonic vortex. The dashed circle corresponds to the corotation radius $r_{\rm c}$, and the dotted–dashed line corresponds to the outer Lindblad resonance (OLR). It is seen that the corotation circle passes through the center of the anticyclone, in agreement with the theory of density waves [77].

We note that (1) the whole spiral-vortex structure rotates with the period $T^{(m=1)} \equiv 2\pi/\Omega_{\rm ph}^{(m=1)} \simeq T_1 \simeq (1/5)P_{\rm orb}$ in the same sense (counterclockwise) as the accretion disk, such that the spiral density wave is lagging; (2) the phase curve of the density wave rotates through $\pi/2$ in the positive direction in the interval $(r_{\rm c}, r_{\rm OLR})$; and (3) the center of the anticyclonic vortex in the perturbed vector velocity field is located, as previously mentioned, at the corotation circle, and rotates together with the spiral density wave at the same angular velocity $\Omega_{\rm ph}^{(m=1)}$. It plays an important role in redistributing the angular momentum of the disk.

All large-scale modes explored here share a similar feature: they are localized in the vicinities of their corotation radii. These radii are close to each other, are located in the internal part of the disk, and can be approximated as

$$r_{\rm c}^{(m)} \simeq r_{\rm c}^{(1)}(1+\beta)^{m-1}\,, \qquad r_{\rm c}^{(1)} \simeq 0.25A\,,$$
$$\beta \simeq 0.024\,, \qquad m = 1,2,3\,.$$

These quantities are close to $r_{\rm c}^{(1)} \simeq 0.21A$ estimated from three-dimensional simulations. The rotational frequencies can be approximated as [10]

$$\omega_{\rm r}^{(m)} \equiv 2\pi f^{(m)} \equiv m\Omega_{\rm ph}^{(m)} \simeq m\Omega_{\rm ph}^{(1)}(1+\beta_1)^{-(m-1)}\,,$$
$$\beta_1 \simeq 0.045\,.$$

Hence, it follows for some frequency shifts that

$$\Delta f^{(m)} \equiv \frac{f^{(m)} - mf^{(1)}}{f^{(m)}} \simeq -\beta_1(m-1)\,; \qquad m = 2,3\,.$$

The results described above for the model of a two-dimensional isolated accretion disk with real parameters, coinciding with those of the three-dimensional model of an accretion disk in a close system of binary stars, are not unexpected. The observed rotation velocity of the 'nuclear' ionized disk at the center of the Galaxy also shows a smoothed slope jump in the vicinity of the radius 0.9 ps (Fig. 18a). Such a shape of the rotation velocity dependence owes its existence to the presence of a massive black hole in the disk center, which is surrounded by an 'isothermal' spherical constellation [11] with the density $\rho_0 \propto r^{-2}$. Numerical simulation [92] shows that the single-arm 'mini-spiral' observed in the nuclear disk can be caused by the overreflection instability excited through the presence of a smoothed jump in the rotation velocity. We note for clarity that (1) only two of four structures of the mini-spiral belong to the nuclear disk: The North Arm and West Arch (Fig. 18b); and (2) the nuclear disk is inclined to the observer's sight by the angle $\sim 60°$. Figure 18b demonstrates the good agreement between the observational data and the results of numerical simulation [92].

4.2 Estimated turbulent viscosity coefficients and the quantity α in accretion disks

In monographs and reviews on plasma physics, the estimate of the turbulent viscosity coefficient $\nu_{\rm turb}$ is written as

$$\nu_{\rm turb} \approx \frac{(\gamma_{\rm L})_{\rm max}}{(k_\perp^2)_{\rm min}} \qquad (29)$$

[10] For purely Kepler's rotation, $\omega_{\rm r}^{(m)} \simeq m\Omega_{\rm ph}^{(1)}(1+\beta)^{-3(m-1)/2}$.

[11] The black hole in the center of the Galaxy causes Keplerian rotation $v_{0\phi} \sim r^{-1/2}$, while the spherical constellation gives $v_{0\phi} = {\rm const}$.

(see, e.g., Ref. [93]), where $(\gamma_L)_{max}$ is the maximum increment of linear instability that leads to the respective turbulent viscosity and $(k_\perp)_{min}$ is the minimum wave number that corresponds to the maximum wavelength generated by this instability.

Formula (29) can be readily derived from dimensional considerations. Indeed, the dimension of the turbulent viscosity ν_{turb}, as well as the molecular viscosity ν_{mol}, is

$$[\nu_{turb}] = [\nu_{mol}] = \mathrm{cm}^2\ \mathrm{s}^{-1}\,.$$

Substituting quantities with the appropriate dimensions in the right-hand side of this expression, $[\mathrm{cm}^2] = [k^{-2}]$, and $[\mathrm{s}^{-1}] = [\gamma]$, we arrive at formula (29).

The presence of a well-developed Kolmogorov turbulence in accretion disks implies that the maximum size of turbulent pulsations is much smaller than the disk half-thickness h, i.e., $k_\perp h \gg 1$, or, in the limit case, $(k_\perp)_{min}\, h \geqslant 1$. With the estimate for the maximum increment of overreflection instability for the $m = 1$ mode (Fig. 17e) and the condition of disk equilibrium in the z-direction, $h \approx c_0/\Omega_0$, we then obtain

$$(\gamma_L)_{max} \simeq 0.035\,\Omega_{ph} = 0.035\,\Omega_{cor} = 3.5\times 10^{-2}\left(\frac{c_0}{h}\right),$$
$$(k_\perp)_{min} \approx h^{-1}\,.$$

Substituting these expressions in Eqn (29), we obtain the turbulent viscosity coefficient

$$\nu_{turb} \approx 3.5\times 10^{-2}\, c_0 h\,.$$

Following [41, 42], we find

$$\alpha \approx 3.5\times 10^{-2}\,,$$

which agrees both with the interval of numerical viscosity in our computations, $10^{-2} < \alpha < 10^{-1}$, and with the interval of α reported in observations and by theoreticians (see, e.g., Refs [50, 52, 94, 95]).

4.3 Turbulence spectrum

It is well known that the Kolmogorov scenario of well-developed stationary turbulence predicts the energy transfer from small to large wave numbers $k_\perp$. The energy flux per unit mass remains constant in this scenario:

$$\varepsilon \approx (\delta V)^2 t^{-1} \approx (\delta V)^3 \lambda^{-1} = \mathrm{const}\,. \qquad (30)$$

Here, it is assumed that turbulent fluctuations at the spatial scale $\sim\lambda$ imply characteristic velocity fluctuations δV.[12] From (30), we derive the well-known Kolmogorov–Obukhov spectrum of turbulence [97, 98]

$$\delta V \approx (\lambda\varepsilon)^{1/3}\,, \qquad \varepsilon = \mathrm{const}\,.$$

We note that condition (30) is valid only for homogeneous and isotropic turbulence, which is not the case for the accretion disks explored here, which are inhomogeneous and rotate differentially.

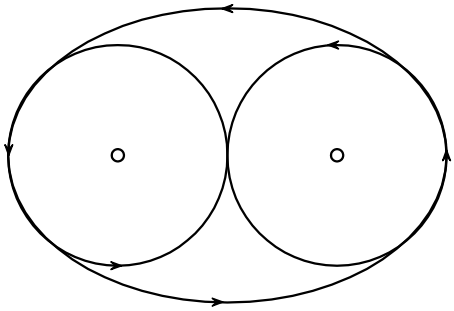

Figure 19. A schematic showing two vortices in shallow water. Their characteristic feature is the tendency to merge into a single vortex.

If one immerses both hands in a vessel with shallow water and rotates them in the same sense one observes two vortices that tend to merge into a single vortex (Fig. 19), i.e., the characteristic scale in this case increases, opposite to the scale in the Kolmogorov cascade, which decreases. This case corresponds to the two-dimensional, Kraichnan–Batchelor–Leith turbulence, for which the condition $k_\perp h \ll 1$ or $(k_\perp)_{max} h \leqslant 1$, opposite to the Kolmogorov one, holds.

As we saw in Section 3.4.4, the visible amplitude of variations in the noneclipsed part of brightness curves varies with the period $T_1 \simeq (1/5)T_{orb}$ (where T_{orb} is the orbital period of a binary system).[13] These variations are most expressed in the emission line of double ionized HeII 4686 Å (see Fig. 16). In the system IP Peg, the orbit inclination angle is $\sim 68^\circ$, and hence the colder and denser part (the single-arm density wave) periodically covers the internal hot region from the observer. This explains the visible variations at non-eclipsed parts of brightness curves. The line HeII 4686 Å originates in the internal parts of the disc with a high temperature exceeding the HeII ionization threshold $\simeq 51$ eV. Analyzing the brightness variations of this line allows understanding the structures that screen the radiation in the outer parts of the accretion disk.

In agreement with the results described in Section 4.1, the single-arm spiral density wave in the accretion disk can be excited by the overreflection instability. This dense structure is localized in the radial range $r \sim (0.15-0.30)A$ and has a period close to T_1.

We represent the density in the equatorial plane of the accretion disk ($z = 0$) at some radius r and for a fixed azimuth angle φ as

$$\rho(t) = \langle\rho\rangle + \Delta\rho(t)\,, \qquad \Delta\rho(t) = \delta\rho_{tdl}(t) + \sum_{m=1}^{m_{max}} \delta\rho^{(m)}(t)\,.$$

Here, we assume that density variations around the mean level $\langle\rho\rangle$ are a superposition of the tidal harmonic $\delta\rho_{tdl}(t)$ and principal eigenmodes in the azimuth direction m ($m_{max} \leqslant 3-4$) generated by the overreflection instability. We can similarly write the observed intensity of radiation in the line HeII 4686 Å as a superposition of the mean value $\langle I\rangle$ and fluctuations $\Delta I(t)$ around it, i.e.,

$$I(t) = \langle I\rangle + \Delta I(t)\,, \qquad \Delta I(t) = \delta I_{tdl}(t) + \sum_{m=1}^{m_{max}} \delta I^{(m)}(t)\,.$$

[12] A comprehensive description of turbulent motion as the superposition of mean and fluctuating components can be found, e.g., in [96].

[13] Obviously, large-amplitude tidal variations are also present. Their period is $T_{tdl} \simeq T_{orb}/2$.

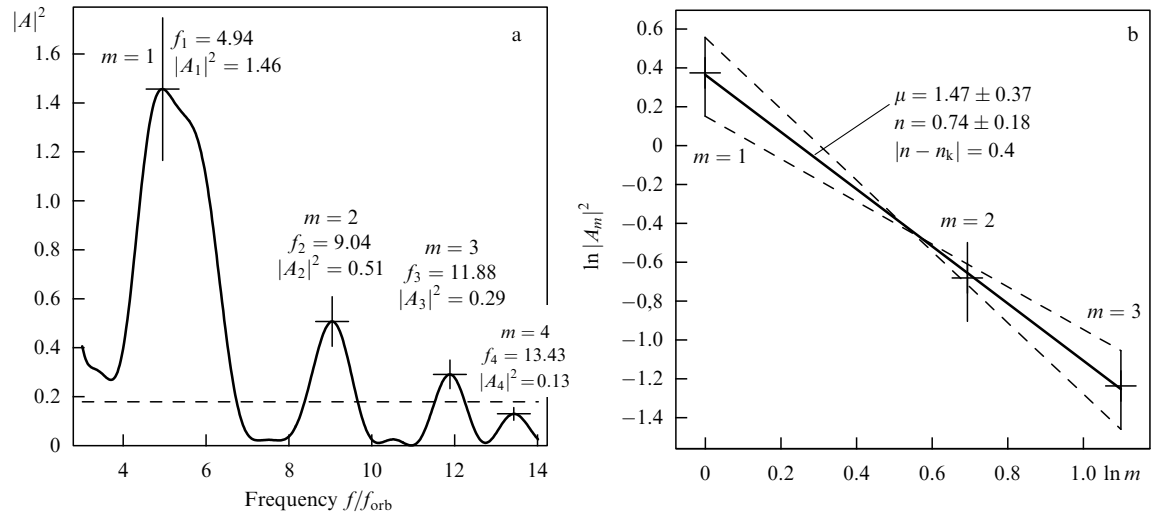

Figure 20. (a) The Fourier spectrum of a fluctuating part of the brightness for the system IP Peg in line HeII 4686 Å (the first night in Fig. 16). The horizontal dashed line marks the level where the observed signal/noise ratio is equal to one. (b) Linear representation of the power law spectrum. The dashed lines give limits which correspond to maximum errors.

Here, $\delta I_{\rm tdl}(t)$ is the tidal harmonic with the frequency $f_{\rm tdl} \simeq 2f_{\rm orb}$, $f_{\rm orb} \equiv 1/T_{\rm orb}$. Other fluctuations correspond to the principal eigenmodes and have a simple harmonic dependence,

$$\delta I^{(m)}(t) \cong A_m \cos\left[2\pi f_m (t - t_{0m})\right] .$$

In this way, the amplitude of the mth harmonic A_m should be proportional to the amplitude $|\delta\rho^{(m)}|$ of the respective eigenmode, $A_m \equiv A(k_\perp^{(m)}) \propto |\delta\rho^{(m)}|$. The Fourier spectrum [99] (the absolute value of the amplitude squared $|A_m|^2$ of the normalized orbital frequency $f_{\rm orb}$) of fluctuations $\Delta I(t)$ shows four main peaks, in addition to the tidal harmonic (Fig. 20a). The first peak at the frequency $f_1 \simeq 4.94$ is presumably related to the $m = 1$ mode. Accordingly, in agreement with the results of our linear stability analysis for an isolated two-dimensional accretion disk with the main parameters of a three-dimensional disk in a binary system (see Section 4.1), the next two peaks should correspond to the modes $m = 2$ and $m = 3$.[14]

The magnitude of specific thermal (elastic) energy of the mth harmonic of the density wave can be estimated as

$$\delta E_{\rm T}^{(m)} \cong \frac{c_0^2}{2\langle\rho\rangle} \left(\delta\rho^{(m)}\right)^2 \propto \left(\delta\rho^{(m)}\right)^2$$

(see, e.g., Ref. [100]). The specific kinetic energy in the same wave is expressed as [100]

$$\delta E_{\rm K}^{(m)} \cong \frac{\langle\rho\rangle}{2} \left(\delta V^{(m)}\right)^2 \propto \left(\delta V^{(m)}\right)^2$$

where $\delta V^{(m)}$ is the velocity perturbation amplitude in the mth-wave harmonic. According to Ref. [100], $\delta E_{\rm T}^{(m)} \simeq \delta E_{\rm K}^{(m)}$, and hence

$$\delta E_{\rm T}^{(m)}\, {\rm d}k \propto \left|\delta\rho^{(m)}\right|^2 \propto \left|A(k_\perp^{(m)})\right|^2 .$$

[14] Frequency shifts in the spectrum shown in Fig. 20a are estimated as $\Delta f^{(2)} \simeq -0.09$ and $\Delta f^{(3)} \simeq -0.25$. They are in qualitative agreement with the results obtained in our model.

Assuming that spectral amplitudes of the maxima follow a power law, we can write

$$(\delta V^{(m)})^2 \propto \left|A(k_\perp^{(m)})\right|^2 \simeq \frac{B}{(k_\perp^{(m)})^{\mu}} \simeq \frac{\tilde{B}}{m^{\mu}} , \qquad (31)$$

where

$$k_\perp^{(m)} \simeq k_\varphi^{(m)} \simeq \frac{m}{r_{\rm c}^{(m)}} \simeq \frac{m}{r_{\rm c}^{(1)}} (1 + \beta)^{-(m-1)} , \qquad m = 1, 2, 3 ,$$

and the corotation radii $r_{\rm c}^{(m)}$ of large-scale modes are assumed to be close to each other (in agreement with results in Section 4.1, we can take $\beta \sim 0.05 \ll 1$).

Taking the logarithm of (31), we obtain

$$\ln\left\{|A_m|^2\right\} \simeq \ln\tilde{B} - \mu \ln m .$$

As is apparent from Fig. 20b, the three peaks corresponding to the modes $m = 1, 2, 3$ follow a linear law (with reasonable accuracy). The slope of this linear dependence gives the following value for the power-law exponent n:

$$\delta V^{(m)} \propto (k_\perp^{(m)})^{-n} , \qquad n \equiv \frac{\mu}{2} \simeq 0.74 \pm 0.18 .$$

The estimated error corresponds to the ambiguity of the computed (using the discrete Fourier transform) power-law spectrum shown with crosses in Fig. 20.

The exponent $n \simeq 0.74 \simeq 3/4$ computed for the accretion disk in IP Peg is substantially different from the exponent of the well-developed turbulence $n_{\rm K} = 1/3$ computed by Kolmogorov and Obukhov, $\Delta n \simeq 0.4$. Such a large difference arises because no accretion disk satisfies two conditions implicit in the Kolmogorov – Obukhov spectrum: the homogeneity and the isotropy.

5. Conclusion

The following main results were obtained in a combined analysis of large-scale processes in accretion disks of binary stars, including three-dimensional numerical simulations, a

numerical solution of the boundary value problem to determine eigenfunctions and eigenfrequencies of a two-dimensional isolated accretion disk with parameters inherited from three-dimensional computations, and Fourier analysis of the power-law spectrum of fluctuations of the noneclipsed part of the brightness curve for the accretion disk IP Peg.

(1) The presence of the global tidal $m = 2$ mode caused by the gravitational influence of the donor star on the accretion disk is demonstrated.

(2) The existence of increasing global oscillatory modes $m = 1, 2, 3$ caused by the overreflection instability is revealed.

(3) The maximum increment $\gamma \simeq 0.035\,\Omega_{\rm ph}$ is shown to be achieved for the first mode $m = 1$.

(4) The maximum instability increment computed by us and the estimate of the minimum magnitude of the wave vector $(k_\perp)_{\rm min} \simeq h^{-1}$ have allowed us for the first time to obtain the turbulent viscosity coefficient and the parameter $\alpha = 0.035$ from first principles. This value of α agrees with the observational and theoretical estimates of many authors.

(5) For the first time, the spectrum of developed turbulence in the accretion disk of the system IP Peg was determined. It follows a power law with the exponent $n \simeq 3/4$.

Acknowledgements

This work was carried out with financial support from the Russian Foundation for Basic Research, the Program of the President of the Russian Federation to support leading scientific schools, programs of the Presidium of the RAS: 'The origin and evolution of stars and galaxies' and 'Mathematical modeling and intellectual systems,' and the Program of the Physical Sciences Branch of the RAS 'Extended objects in the Universe.'

References

1. Masevich A G, Tutukov A V *Evolyutsiya Zvezd*: *Teoriya i Nablyudeniya* (Evolution of Stars: The Theory and Observations) (Moscow: Nauka, 1988)
2. Landau L D, Lifshitz E M *Mekhanika* 4th ed. (Mechanics) (Moscow: Nauka, 1988) [Translated into English (Oxford: Pergamon Press, 1980)]
3. Szebehely V *Theory of Orbits*: *the Restricted Problem of Three Bodies* (New York: Academic Press, 1967)
4. Papaloizou J, Pringle J E *Mon. Not. R. Astron. Soc.* **181** 441 (1977)
5. Lin D N C, Papaloizou J C B, Savonije G J *Astrophys. J.* **365** 748 (1990)
6. Dgani R, Livio M, Regev O *Astrophys. J.* **436** 270 (1994)
7. Michel F C *Astrophys. J.* **279** 807 (1984)
8. Sawada K, Matsuda T, Hachisu I *Mon. Not. R. Astron. Soc.* **219** 75 (1986)
9. Spruit H C *Astron. Astrophys.* **184** 173 (1987)
10. Syer D, Narayan R *Mon. Not. R. Astron. Soc.* **262** 749 (1993)
11. Bisnovatyi-Kogan G S, Blinnikov S I *Pis'ma Astron. Zh.* **2** 489 (1976) [*Sov. Astron. Lett.* **2** 191 (1976)]
12. Paczyński B *Comments Astrophys.* **6** 95 (1976)
13. Shakura N I, Sunyaev R A, Zilitinkevich S S *Astron. Astrophys.* **62** 179 (1978)
14. Lin D N C, Papaloizou J *Mon. Not. R. Astron. Soc.* **191** 37 (1980)
15. Blandford R D, Payne D G *Mon. Not. R. Astron. Soc.* **199** 883 (1982)
16. Lubow S H, Papaloizou J C B, Pringle J E *Mon. Not. R. Astron. Soc.* **268** 1010 (1994)
17. Cao X, Spruit H C *Astron. Astrophys.* **385** 289 (2002)
18. Lynden-Bell D *Mon. Not. R. Astron. Soc.* **341** 1360 (2003)
19. Lin D N C, Papaloizou J *Mon. Not. R. Astron. Soc.* **186** 799 (1979)
20. Lubow S H *Astrophys. J.* **245** 274 (1981)
21. Vishniac E T, Diamond P *Astrophys. J.* **347** 435 (1989)
22. Velikhov E P *Zh. Eksp. Teor. Fiz.* **36** 1398 (1959) [*Sov. Phys. JETP* **9** 995 (1959)]
23. Chandrasekhar S *Hydrodynamic and Hydromagnetic Stability* (New York: Dover Publ., 1981)
24. Balbus S A, Hawley J F *Astrophys. J.* **376** 214 (1991)
25. Winters W F, Balbus S A, Hawley J F *Mon. Not. R. Astron. Soc.* **340** 519 (2003)
26. Goodman J *Astrophys. J.* **406** 596 (1993)
27. Lubow S H, Pringle J E, Kerswell R R *Astrophys. J.* **419** 758 (1993)
28. Cabot W *Astrophys. J.* **277** 806 (1984)
29. Li H et al. *Astrophys. J.* **533** 1023 (2000)
30. Klahr H H, Bodenheimer P *Astrophys. J.* **582** 869 (2003)
31. Papaloizou J C B, Lin D N C *Annu. Rev. Astron. Astrophys.* **33** 505 (1995)
32. Balbus S A *Annu. Rev. Astron. Astrophys.* **41** 555 (2003)
33. Fridman A M et al. *Phys. Lett. A* **317** 181 (2003)
34. Paczyński B, Sienkiewicz R *Acta Astron.* **22** 73 (1972)
35. Lubow S H, Shu F H *Astrophys. J.* **198** 383 (1975)
36. Shore S N, Livio M, van den Heuvel E P J *Interacting Binaries* (Saas-Fee Adv. Course, Lecture Notes, 1992, No. 22, Eds H Nussbaumer, A Orr) (Berlin: Springer-Verlag, 1994)
37. Boyarchuk A A, Bisikalo D V, Kuznetsov O A, Chechetkin V M *Mass Transfer in Close Binary Stars* (Adv. in Astron. and Astrophys., Vol. 6) (London: Taylor & Francis, 2002)
38. Warner B *Cataclysmic Variable Stars* (Cambridge: Cambridge Univ. Press, 1995)
39. Pringle J E, in *Interacting Binary Stars* Ch. 1 (Cambridge Astrophys. Ser., Vol. 6, Eds J E Pringle, R A Wade) (Cambridge: Cambridge Univ. Press, 1985)
40. Bath G T, Pringle J E "Cataclysmic variables: An theoretical review", in *Interacting Binary Stars* (Cambridge Astrophys. Ser., Vol. 6, Eds J E Pringle, R A Wade) (Cambridge: Cambridge Univ. Press, 1985)
41. Shakura N I *Astron. Zh.* **49** 921 (1972) [*Sov. Astron.* **16** 756 (1973)]
42. Shakura N I, Syunyaev R A *Astron. Astrophys.* **24** 337 (1973)
43. Frank J, King A R, Raine D J *Accretion Power in Astrophysics* (Cambridge: Cambridge Univ. Press, 1985)
44. Fridman A M, Polyachenko V L *Physics of Gravitating Systems* (New York: Springer-Verlag, 1984)
45. Fridman A M, Gor'kavyi N N *Fizika Planetnykh Kolets* (Physics of Planetary Rings) (Moscow: Nauka, 1994) [Translated into English (New York: Springer, 1999)]
46. Mineshige S, Wheeler J C (Eds) *Disk Instabilities in Close Binary Systems*: *25 Years of the Disk-Instability Model* (Frontiers Sci. Ser., No. 26) (Tokyo: Universal Academy Press, 1999)
47. Pringle J E *Annu. Rev. Astron. Astrophys.* **19** 137 (1981)
48. Popham R, Narayan R *Astrophys. J.* **370** 604 (1991)
49. Fridman A M, Khoruzhii O V, in: Fridman A M, Gor'kavyi N N *Fizika Planetnykh Kolets* (Physics of Planetary Rings) (Moscow: Nauka, 1994) p. 282
50. Lynden-Bell D, Pringle J E *Mon. Not. R. Astron. Soc.* **168** 603 (1974)
51. Verbunt F "Accretion disks in stellar X-ray sources — A review of the basic theory of accretion disks and its problems" *Space Sci. Rev.* **32** 379 (1982)
52. Meyer-Hofmeister E, Ritter H "Accretion disks in close binaries", in *The Realm of Interacting Binary Stars* (Astrophys. and Space Sci. Library, Vol. 177, Eds J Sahade, G E McCluskey (Jr.), Y Kondo) (Dordrecht: Kluwer Acad. Publ., 1993) p. 143
53. Tout C "Accretion disk viscosity", in *Cataclysmic Variables and Related Objects* (Astrophys. and Space Sci. Library, Vol. 208, Eds A Evans, J H Wood) (Dordrecht: Kluwer Acad. Publ., 1996) p. 97
54. Alexander D R, Augason G C, Johnson H R *Astrophys. J.* **345** 1014 (1989)
55. Bell K R, Lin D N C *Astrophys. J.* **427** 987 (1994)
56. Cannizzo J K, Kenyon S J *Astrophys. J. Lett.* **309** L43 (1986)
57. Cox D P, Daltabuit E *Astrophys. J.* **167** 113 (1971)
58. Raymond J C, Cox D P, Smith B W *Astrophys. J.* **204** 290 (1976)
59. Spitzer L (Jr.) *Physical Processes in the Interstellar Medium* (New York: Wiley, 1978) [Translated into Russian (Moscow: Mir, 1981)]
60. Schwarzschild M *Structure and Evolution of the Stars* (Princeton: Princeton Univ. Press, 1958) [Translated into Russian (Moscow: IL, 1961)]

61. Bisnovatyi-Kogan G S *Fizicheskie Voprosy Teorii Zvezdnoi Evolyutsii* (Physical Problems of the Stellar Evolution Theory) (Moscow: Nauka, 1989) [Translated into English: *Stellar Physics* (Berlin: Springer-Verlag, 2001)]
62. Nagasawa M, Matsuda T, Kuwahara K *Numer. Astrophys. Jpn.* **2** 27 (1991)
63. Hirose M, Osaki Y, Mineshige S *Publ. Astron. Soc. Jpn.* **43** 809 (1991)
64. Molteni D, Belvedere G, Lanzafame G *Mon. Not. R. Astron. Soc.* **249** 748 (1991)
65. Bisikalo D V et al. *Astron. Zh.* **78** 707 (2001) [*Astron. Rep.* **45** 611 (2001)]
66. Molteni D et al. *Mon. Not. R. Astron. Soc.* **327** 1103 (2001)
67. Bisikalo D V et al. *Astron. Zh.* **80** 879 (2003) [*Astron. Rep.* **47** 809 (2003)]
68. Bisikalo D V et al. *Astron. Zh.* **81** 494 (2004) [*Astron. Rep.* **48** 449 (2004)]
69. Bisikalo D V et al. *Astron. Zh.* **81** 648 (2004) [*Astron. Rep.* **48** 588 (2004)]
70. Bisikalo D V *Astrophys. Space Sci.* **296** 391 (2005)
71. Bisikalo D V et al. *Astron. Zh.* **82** 788 (2005) [*Astron. Rep.* **49** 701 (2005)]
72. Bisikalo D V et al. *Chin. J. Astron. Astrophys.* **6** 159 (2006)
73. Lyubarskij Yu E, Postnov K A, Prokhorov M E *Mon. Not. R. Astron. Soc.* **266** 583 (1994)
74. Ogilvie G I *Mon. Not. R. Astron. Soc.* **325** 231 (2001)
75. Bisikalo D V et al. *Astron. Zh.* **78** 780 (2001) [*Astron. Rep.* **45** 676 (2001)]
76. Fridman A M, Khoruzhii O V *Space Sci. Rev.* **105** 1 (2003)
77. Fridman A M *Usp. Fiz. Nauk* **177** 121 (2007) [*Phys. Usp.* **50** 115 (2007)]
78. Gorbatskii V G *Astrofiz.* **3** 245 (1967) [*Astrophys.* **3** 116 (1967)]
79. Smak J *Acta Astron.* **20** 311 (1970)
80. Khruzina T S et al. *Astron. Zh.* **78** 625 (2001) [*Astron. Rep.* **45** 538 (2001)]
81. Khruzina T S et al. *Astron. Zh.* **80** 675 (2003) [*Astron. Rep.* **47** 621 (2003)]
82. Khruzina T S et al. *Astron. Zh.* **80** 919 (2003) [*Astron. Rep.* **47** 848 (2003)]
83. Khruzina T S et al. *Astron. Zh.* **82** 99 (2005) [*Astron. Rep.* **49** 79 (2005)]
84. Mason K O, Drew J E, Knigge C *Mon. Not. R. Astron. Soc.* **290** L23 (1997)
85. Froning C S, Long K S, Knigge C *Astrophys. J.* **584** 433 (2003)
86. Marsh T R, Horne K *Mon. Not. R. Astron. Soc.* **235** 269 (1988)
87. Kuznetsov O A et al. *Astron. Zh.* **78** 997 (2001) [*Astron. Rep.* **45** 872 (2001)]
88. Morales-Rueda L, Marsh T R, Billington I *Mon. Not. R. Astron. Soc.* **313** 454 (2000)
89. Wolf S et al. *Astron. Astrophys.* **332** 984 (1998)
90. Paczyński B *Astrophys. J.* **216** 822 (1977)
91. Lyakhovich V V, Fridman A M, Khoruzhii O V, in *Neustoichivye Protsessy vo Vselennoi* (Unstable Processes in the Universe) (Executive Ed. A G Mosevich) (Moscow: Kosmosinform, 1994) p. 194
92. Fridman A M et al., in *The Galactic Center* (Astron. Soc. of the Pacific Conf. Ser., Vol. 102, Ed. R Gredel) (San Francisco: ASP, 1996) p. 335
93. Kadomtsev B B, in *Voprosy Teorii Plazmy* (Reviews in Plasma Physics) Vol. 4 (Ed. M A Leontovich) (Moscow: Atomizdat, 1964) p. 188 [Translated into English (New York: Consultants Bureau, 1966)]
94. Smak J *Acta Astron.* **49** 391 (1999)
95. Shu F H et al. *Astrophys. J.* **665** 535 (2007)
96. Monin A S, Yaglom A M *Statisticheskaya Gidrodinamika* (Statistical Fluid Mechanics) (Moscow: Nauka, 1964, 1967) [Translated into English: Vol. 1, 2 (Cambridge, MA: MIT Press, 1971, 1975)]
97. Kolmogorov A N *Dokl. Akad. Nauk SSSR* **30** 301 (1941) [*C.R. Acad. Sci. URSS* **30** 301 (1941)]
98. Obukhov A M *Dokl. Akad. Nauk SSSR* **32** 22 (1941) [*C.R. Acad. Sci. URSS* **32** 22 (1941)]
99. Fridman A M et al., in *Chaos in Astronomy 2007* (Eds P Patsis, G Contopoulos) (Berlin: Springer-Verlag, 2008) (in press)
100. Landau L D, Lifshitz E M *Gidrodinamika* (Fluid Mechanics) (Moscow: Nauka, 1986) [Translated into English (Oxford: Pergamon Press, 1987)]